Memoirs of the School of Engineering, Nagoya University
Vol.47, No.1 (1995)

WAVE FORCE ACTING ON A SUBMERGED SPHERE

Koichiro IWATA and Norimi MIZUTANI

Department of Civil Engineering

(Received May 26, 1995)

Abstract

Wave force acting on a submerged sphere is discussed experimentally and theoretically. This paper consists of major two parts. One is the wave force on a sphere with large diameter, in which the diffraction force is a predominant wave force. The other one is the wave force on a small sphere. In this case, the inertia, drag and lift forces are the major components of the wave force. These forces are governed by a flow around a sphere, and therefore the characteristics of them are discussed experimentally in relation to the results of flow visualizing experiment. The drag and inertia coefficients in the Morison equation are well formulated in this paper. Moreover, new wave force formulae are proposed to enable to evaluate the wave force affected by the proximity effects of the bottom and free surface boundaries. This paper also shows that the applicability of these wave force formulae together with their simplified formulae.

Contents

1. General

Exact estimation of the wave force acting on coastal and offshore structures is one of the most important problems for field engineers. Many researches have been conducted on the wave forces acting on a circular cylinder[1]. However, only a few investigations have been performed for the wave forces acting on a submerged sphere[2),3),4)]. Since the wave pressure acting on the object is generally isotropic, the sphere may be regarded as one of the most suitable shapes for an intermediate buoy in a mooring system for floating structures, underwater storage tanks, etc. Therefore, it is important to investigate the characteristics of the wave forces acting on a sphere to establish a rational engineering design formula for this kind of structure.

Wave force can be classified into four components from their generation mechanisms. One is the diffraction force and others are the inertia, the drag and the lift forces. The diffraction force is very significant in case that the size of an object is large compared with the wavelength, whereas other three components are important for small objects. For a large object, the existence of an object causes the wave deformation, and therefore a change of the pressure distribution in time and space on the surface takes place. The resultant force is called the diffraction force and we have to evaluate the wave deformation in order to estimate the diffraction force. On the other hand, when an object is small compared with the wavelength, the inertia, drag and lift forces are dominant force components. In this case, the wave deformation is negligibly small, while the flow field including vortex shedding around an object is very important. The role of each component on the total force depends much on the flow condition, in particular on the flow separation and vortex shedding. It is very difficult to solve theoretically the flow condition around a small object, and therefore we have to discuss these forces based on the hydraulic experiments. Thus, the quite different treatments are necessary to discuss the wave forces on large and small objects.

In this paper, the wave force under regular wave excitation is discussed. The diffraction force on a large sphere is first discussed in the following chapter (Chapter 2) together with the range in which the wave diffraction should be considered. Next, in Chapter 3, wave forces acting on a small sphere are investigated. The proximity effects of the bottom and free surface boundaries on the wave force are also investigated so that the new estimation formulae can be established. Finally, the results obtained in this study are summarized in Chapter 4.

2. Wave Force Acting on a Submerged Sphere with Large Diameter

2. 1 *Introduction*

In this chapter, the diffraction force which is the dominant wave force component for the acting wave force on large objects is investigated. Under such a condition, flow separation hardly occurs and its effect can be neglected. Therefore, the motion of water is approximated as an irrotational one and analysis based on the velocity potential can be applied. The wave force, then, can be evaluated by integrating the wave pressure, derived from the velocity potential, on the wetted surface. Thus, the objective of this chapter is equivalent to obtain the velocity potential of diffracted waves. Even in such background, the research which has been conducted on the diffraction force acting on the spherical structure is quite limited compared with those of the cylindrical structures. Havelock[5] discussed the diffraction force acting on a submerged sphere under the deep water wave condition. His theory, however, is derived without taking the free surface boundary condition into account, and therefore it is impossible to evaluate the effects of the bottom and free surface boundaries on the acting wave force. The effect of the free surface was discussed in the case of a bottom-seated hemisphere[6),7)]. They reported that the effect of the free surface boundary on the wave force is negligibly small if the radius of hemisphere is less than half of the stillwater depth. Black[8] discussed theoretically the diffraction force on a sphere with its center being on the stillwater level. He developed the numerical analyzing method using the axisymmetric Green's function and concluded that the bottom boundary affects little the wave force in the case that the water depth is larger than twice of the sphere radius. Similar results were obtained by Fenton[9]. Concerning the diffraction force acting on a fully submerged sphere in the finite water depth, there have been very few analytical investigations taking the bottom and free surface boundary conditions into consideration.

In this chapter, the velocity potential of the diffracted wave is obtained by numerical analysis in which the Source Distribution Method is employed. Based on the numerical analysis and laboratory experiments, the diffraction force on a submerged sphere and its dominating range are discussed.

2. 2 *Numerical Analysis*

2. 2. 1 *Source Distribution Method*

As shown in Fig. 2.1, a sphere with radius a is fixed in the constant water depth, h. The center of the sphere is located at (x,y,z) = (0,0,−d), where the coordinate system is Cartesian shown in Fig. 2.1. The small amplitude wave with height H_I and angular frequency σ ($= 2\pi/T$, T : the wave period) propagates to the positive direction of x-axis.

Provided that the fluid is inviscid and incompressible and its motion is irrotational, the fluid motion can be represented by the velocity potential, Φ given in Eq.(2.1).

$$\Phi = (\phi_I + \phi_S)e^{-i\sigma t} \tag{2.1}$$

where ϕ_I and ϕ_S are the spatial velocity potentials of the incident and diffracted waves, respectively, and $i = \sqrt{-1}$. The velocity potential of the incident wave, ϕ_I can be given by the following form using the spherical coordinate (see Fig. 2.1).

$$\phi_I = -\frac{iH_I\sigma}{2k}\sum_{m=0}^{\infty}\varepsilon_m i^m \frac{\cosh k(s + r\cos\theta)}{\sinh kh} J_m(kr\sin\theta)\cos m\psi \tag{2.2}$$

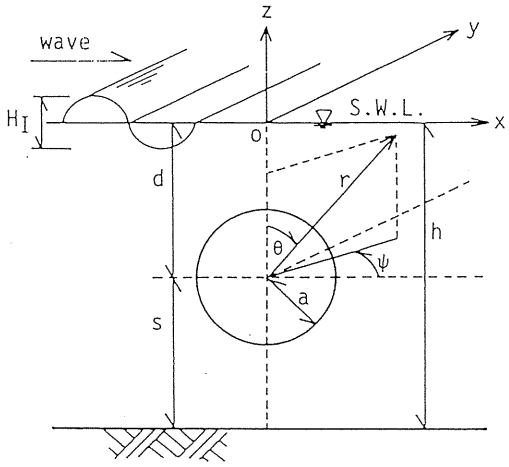

Fig. 2.1 Definition sketch

where, r is the radius vector, θ the zenithal angle, ψ the azimuth angle, $\mathbf{J}_m$ the m-th order Bessel function of the first kind, ε_m the Neumann's constant and k the eigenvalue described in the latter part of this section.

The velocity potential of the diffracted wave, ϕ_S should satisfy the following fundamental equation and boundary conditions.

Fundamental equation:

$$\frac{\partial^2\phi_S}{\partial r^2}+\frac{2}{r}\frac{\partial\phi_S}{\partial r}+\frac{1}{r^2}\frac{\partial^2\phi_S}{\partial\theta^2}+\frac{\cot\theta}{r^2}\frac{\partial\phi_S}{\partial\theta}+\frac{1}{r^2\sin^2\theta}\frac{\partial^2\phi_S}{\partial\psi^2}=0 \tag{2.3}$$

Boundary conditions:

$$\frac{\partial\phi_S}{\partial z}=\frac{\sigma^2}{g}\phi_S \qquad \text{on } z=0 \tag{2.4}$$

$$\frac{\partial\phi_S}{\partial z}=0 \qquad \text{on } z=-h \tag{2.5}$$

$$\frac{\partial\phi_S}{\partial r}=-\frac{\partial\phi_I}{\partial r} \qquad \text{on } r=a \tag{2.6}$$

$$\lim_{r\to\infty}\sqrt{r}\left(\frac{\partial\phi_S}{\partial r}-ik\phi_S\right)=0 \tag{2.7}$$

where, g is the acceleration of gravity.

In this study, the Source Distribution Method (hereafter, referred to as the SDM) is employed in order to determine ϕ_S. In the SDM, ϕ_S is given by Eq.(2.8) as the sum of the

contributions of the individual sources distributed on the sphere surface.

$$\phi_S = \frac{1}{4\pi}\int\int_{R=a} f(R,\Theta,\Psi)G(r,\theta,\psi;R,\Theta,\Psi)ds(R,\Theta,\Psi) \tag{2.8}$$

where (r,θ,ψ) and (R,Θ,Ψ) are, respectively, the coordinates of a reference point and a point source, $G(r,\theta,\psi;R,\Theta,\Psi)$ the Green's function which means the velocity potential due to a point source and $f(R,\Theta,\Psi)$ the source distribution function which represents its strength.

The Green's function satisfying the fundamental equation, Eq.(2.3), and three boundary conditions, Eqs.(2.4), (2.5) and (2.7), is given by following equation[10].

$$\begin{aligned} G(r,\theta,\psi;R,\Theta,\Psi) &= q_0 \cosh k(s + r\cos\theta)\cosh k(s + R\cos\Theta)H_0^{(1)}(kQ) \\ &+ \sum_{n=1}^{\infty} q_n \cosh k_n(s + r\cos\theta)\cosh k_n(s + R\cos\Theta)K_0(k_nQ) \end{aligned} \tag{2.9}$$

where, $\mathbf{H}_0^{(1)}$ and $\mathbf{K}_0$ are the 0-th order Hankel function of the first kind and the modified Bessel function of the second kind, respectively. $\mathbf{Q}$, q_0 and q_n $(n \geq 1)$ are given by the following equations.

$$Q = \sqrt{(r\sin\theta)^2 + (R\sin\Theta)^2 - 2rR\sin\theta\sin\Theta\cos(\psi - \Psi)} \tag{2.10}$$

$$q_0 = \frac{2\pi i\left(k^2 - k_0^2\right)}{\left(k^2 - k_0^2\right)h + k_0} \tag{2.11}$$

$$q_n = \frac{4\left(k_n^2 + k_0^2\right)}{\left(k_n^2 + k_0^2\right)h - k_0} \tag{2.12}$$

In Eqs.(2.2) through (2.11), k_0, k and k_n are eigenvalues which satisfy the dispersion relationships, Eq.(2.13) and Eq.(2.14).

$$k_0 = \sigma^2/g \tag{2.13}$$

$$\frac{\sigma^2}{g} = k\tanh kh = -k_n\tan k_nh \tag{2.14}$$

Once the source distribution function $f(a,\Theta,\Psi)$ is determined so that ϕ_S satisfies the impermeable condition on the sphere surface, Eq.(2.6), the velocity potential of the diffracted wave, $\phi_S(r,\theta,\psi)$ is obtained.

2. 2. 2 Determination of the Source Distribution Function

The source distribution function is determined using Eq.(2.6). The integration cannot be carried out straightforwardly because the Green's function has a singularity at $Q = 0$. To avoid the singularity, the relationship written in Eq.(2.15) is used[6),8)] to determine the source distribution function, in which the first term of the left hand side corresponds to the integration around a singular point.

$$-\frac{1}{2}f(a,\theta,\phi)+\frac{1}{4\pi}\iint_{(a,\theta,\psi)\neq(a,\Theta,\Psi)} f(a,\Theta,\Psi)\frac{\partial G(r,\theta,\psi;a,\Theta,\Psi)}{\partial r}dS(a,\Theta,\Psi)$$

$$+\frac{\partial\phi_I}{\partial r}=0 \qquad \text{at } r=a \tag{2.15}$$

Considering the axisymmetry of the source distribution function, $f(a,\Theta,\Psi)$ can be expanded into a Fourier series.

$$f(a,\Theta,\Psi)=\sum_{m=0}^{\infty} f^{(m)}(a,\Theta)\cos m\Psi \tag{2.16}$$

where, $f^{(m)}$ is the Fourier coefficient of order m.

Using the addition theorem of the cylindrical function and taking account of the axisymmetry with respect to $(\psi\text{-}\Psi)$, the Green's function can be also expanded into a Fourier series.

$$\begin{aligned}G(r,\theta,\psi;a,\Theta,\Psi)&=\sum_{m=0}^{\infty} G^{(m)}(r,\theta;a,\Theta)\cos m(\psi-\Psi)\\&=\sum_{m=0}^{\infty}\varepsilon_m\Bigg\{q_0\cosh k(s+r\cos\theta)\cosh k(s+a\cos\Theta)\\&\qquad\cdot\begin{pmatrix}H_m^{(1)}(kr\sin\theta)J_m(ka\sin\Theta)\\H_m^{(1)}(ka\sin\Theta)J_m(kr\sin\theta)\end{pmatrix}\\&\quad+\sum_{n=1}^{\infty}q_n\cos k_n(s+r\cos\theta)\cos k_n(s+a\cos\Theta)\\&\qquad\cdot\begin{pmatrix}k_m(k_nr\sin\theta)I_m(k_na\sin\Theta)\\k_m(k_na\sin\Theta)I_m(k_nr\sin\theta)\end{pmatrix}\Bigg\}\cos m(\psi-\Psi)\end{aligned} \tag{2.17}$$

where, $G^{(m)}$ is the Fourier coefficient of order m, and I_m is the m-th order modified Bessel function of the first kind. The upper and lower terms in the brackets are to be adopted for $|r\sin\theta|>|a\sin\Theta|$ and $|r\sin\theta|<|a\sin\Theta|$, respectively.

Since the addition theorem is not applicable in the case that $|r\sin\theta|=|a\sin\Theta|$, another treatment is required for this condition. In the past investigations, the mean value of the upper and lower terms were used. The validity of this method, however, has not been discussed enough. Therefore, in this study, the following new method is employed.

Differentiation of Eq.(2.9) with respect to r leads to the following equation in the case that $|r\sin\theta|=|a\sin\Theta|$.

$$\frac{\partial G}{\partial r} = q_0\Big[k\cos\theta\sinh k(s + r\cos\theta)\cosh(s + a\cos\Theta)H_0^{(1)}(kQ^*) - \frac{\sqrt{2}}{2}\cosh k(s + r\cos\theta)\cosh k(s + a\cos\Theta)H_0^{(1)\prime}(kQ^*)\Big] + \sum_{n=1}^{\infty} q_n\Big[(-k_n\cos\theta)\sin k_n(s + r\cos\theta)\cos k_n(s + a\cos\theta)K_0(k_nQ^*) - \frac{\sqrt{2}}{2}\cos k_n(s + r\cos\theta)\cos k_n(s + a\cos\Theta)K_0'(k_nQ^*)\Big] \tag{2.18}$$

in which, $Q^* = \sqrt{2}a\sin\theta\sqrt{1 - \cos(\psi - \Psi)}$ and (′) indicates the differentiation with respect to r. Equation (2.18) can be also expanded numerically into a Fourier series using the axisymmetry with respect to $(\psi - \Psi)$, instead of taking the mean value of the upper and lower terms in the bracket in Eq.(2.17).

$$\frac{\partial G}{\partial r} = \sum_{m=0}^{\infty} G^{(m)}(r,\theta;a,\Theta)\cos m(\psi - \Psi) \tag{2.19}$$

Substituting Eqs.(2.17) and (2.19) into Eq.(2.15) and using the relationship $ds = a^2\sin\Theta d\Theta d\Psi$, the integral equation can be obtained for each mode of the Fourier series. Since the Fourier coefficients $G^{(m)}(r,\theta,a,\Theta)$ and $f^{(m)}(\Theta)$ depend only on θ and Θ in the case of $r = a$, the integral equation is rewritten into the simultaneous linear equations by dividing the sphere surface into many pieces of latitudinal ring by parallels, as shown in Fig. 2.2. Solving the simultaneous linear equations, $f^{(m)}(\Theta)$ can be obtained and then the source distribution function $f(a,\theta,\psi)$ can be determined with use of Eq.(2.16). Consequently, the wave forces in x and z directions, Fx and Fz, are evaluated by the following equations.

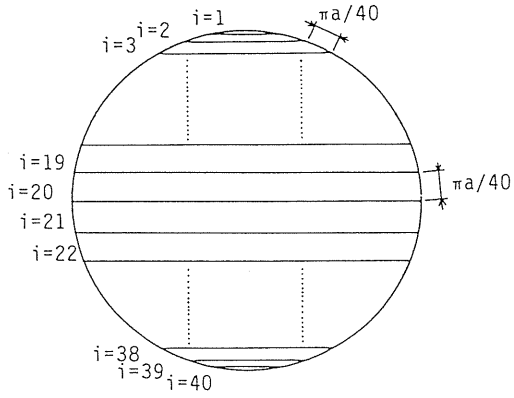

Fig. 2.2 Vertical view of surface elements of sphere

$$Fx = F_{IX} + F_{DX}$$
$$= \mathrm{Real}\left[\left\{i\rho\ \sigma\int \phi_I \sin\theta \cos\psi dS\right\}e^{-i\sigma t}\right] + \mathrm{Real}\left[\left\{i\rho\ \sigma\int \phi_S \sin\theta \cos\psi dS\right\}e^{-i\sigma t}\right] \tag{2.20}$$

$$Fz = F_{IZ} + F_{DZ}$$
$$= \mathrm{Real}\left[\left\{i\rho\ \sigma\int \phi_I \cos\theta dS\right\}e^{-i\sigma t}\right] + \mathrm{Real}\left[\left\{i\rho\ \sigma\int \phi_S \cos\theta dS\right\}e^{-i\sigma t}\right] \tag{2.21}$$

where, ρ is the density of water and F_{Ii} and F_{Di} ($i = x, z$) are, respectively, the wave force due to the incident and the diffracted waves.

Calculations were performed under following conditions which were determined by preliminary calculations[11]. The sphere surface was divided into 40 elements with same width of $\pi a/40$ as shown in Fig. 2.2. The evanescent mode waves corresponding to the smallest 15 eigenvalues k_n were taken into account. Concerning the Fourier series, the finite series up to the first 10th mode were adopted.

2. 3 Experimental Set-up and Procedure

Laboratory experiments were carried out using three-dimensional wave basin (30 m in length, 10 m in width and 0.6 m in depth) at Department of Civil Engineering, Nagoya University. Experimental conditions are listed in Table 2.1. As shown in the table, the range of wave steepness H_I/L was from 0.0095 to 0.085 (L : the wavelength) which includes the finite amplitude waves of the second and third order Stokes waves.

Table 2.1 Experimental conditions

h (cm)	41.0			
H_I/h	0.06 - 0.18			
H_I/L	0.0095 - 0.085			
h/gT^2	0.013, 0.035, 0.065, 0.074, 0.102, 0.167			
D/h	0.902	0.733	0.488	0.293
d/h	0.50	0.50	0.39 0.50	0.293 0.39 0.50

In each experimental run, the x- and z-directed velocities u and w, wave forces Fx and Fz, and the water surface profiles were simultaneously measured using the electromagnetic-type velocimeter, the cantilever-type wave force meters devised for this experiment and the capacitance-type wave gauges, respectively. The lowest natural frequency of the wave force meter was about 8 Hz and its effect on the measured wave force is negligibly small.

2. 4 *Maximum Wave Force*

The relationships between the non-dimensional maximum wave force ($Fx_m/\rho gD^2H_I$, $Fz_m/\rho gD^2H_I$) and ka are shown in Figs.2.3 and 2.4. The non-dimensional maximum wave forces $Fx_m/\rho gD^2H_I$ and $Fz_m/\rho gD^2H_I$ vary with ka and they take a maximal value, and it is clearly recognized that the variations of $Fx_m/\rho gD^2H_I$ and $Fz_m/\rho gD^2H_I$ with ka become larger as D/h increases.

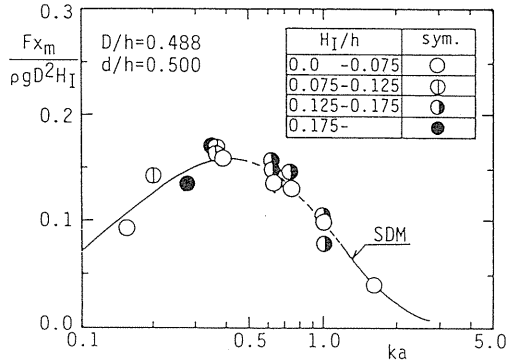

(a) D/h=0.488

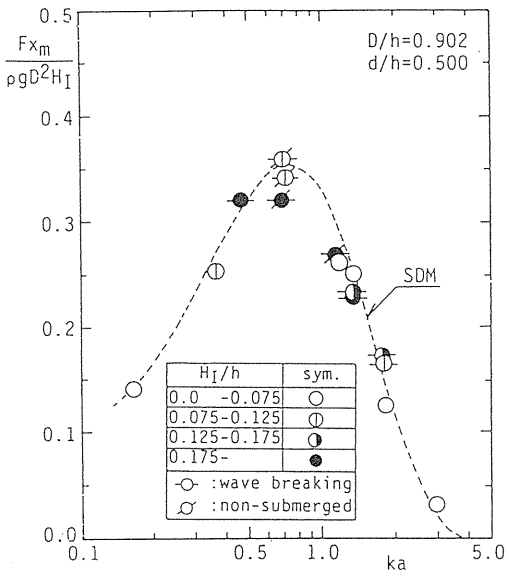

(b) D/h=0.902

Fig. 2.3 Relationship between $Fx_m/\rho gD^2H_I$ and ka

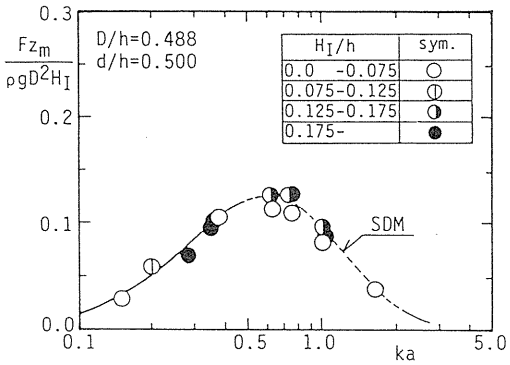

(a) D/h=0.488

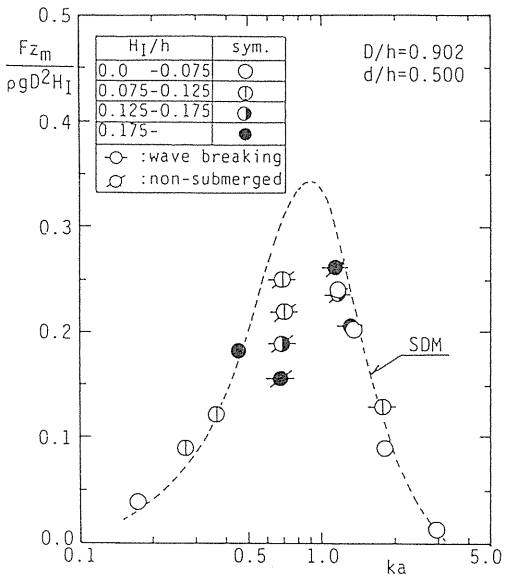

(b) D/h=0.902

Fig. 2.4 Relationship between $Fz_m/\rho gD^2H_I$ and ka

As shown in the figures, it can be pointed out that the agreement between experimental and calculated values of $Fx_m/\rho gD^2H_I$ is generally good and increasing wave height seems to affect little the non-dimensional maximum wave force. Also, calculated values of $Fz_m/\rho gD^2H_I$ agree well with the measured ones under the condition that D/h is less than 0.9. The experimental values of $Fz_m/\rho gD^2H_I$ in case that $D/h = 0.902$ and $0.7 < ka < 1.2$, however, are much smaller than the calculated one and the difference increases with an increment of H_I/h. In these cases, the sphere emerges from the wave trough and the wave pressure never acts on the sphere surface above the free surface. On the contrary, in the analysis, it is assumed that the wave is of small amplitude and the sphere is always below the free surface. Therefore, the wave pressure acts on all over the sphere surface and the whole wave pressure is taken into the calculation of the wave force. This difference causes the discrepancy between the experimental and analytical values. It is worth noting that the effect of appearance of the sphere above the free surface on the horizontal wave force is very small. The reason of this fact is that the most part of wave pressure on the top part of the sphere is the vertical component and the contribution of horizontal component to the total wave force is small. Consequently, the difference between the experimental and analytical values appears clearly in the vertical wave force.

2. 5 Dominant Range of Diffraction Force

In the previous sections, characteristics of the maximum wave force are discussed. Also the SDM, based on the linear wave theory, is effective in estimating the diffraction force except for the vertical wave force when the sphere emerges from the wave trough. However, we have to know when the SDM is applied, in other words, the range in which the diffraction force is dominant.

The wave force, Fx, can be expressed as follows.

$$\begin{aligned} Fx &= Fx_m \sin(\sigma t + \alpha_{IX}) \\ &= F_{IXm} \sin\sigma t + F_{DXm} \sin(\sigma t + \alpha_{AX}) \\ &= (F_{IXm} + F_{DXm} \cos\alpha_{AX})\sin\sigma t + F_{DXm} \sin\alpha_{AX} \cos\sigma t \end{aligned} \tag{2.22}$$

Similarly,

$$\begin{aligned} Fz &= -Fz_m \cos(\sigma t + \alpha_{IZ}) \\ &= -(F_{IZm} + F_{DZm} \cos\alpha_{AZ})\cos\sigma t + F_{DZm} \sin\alpha_{AZ} \sin\sigma t \end{aligned} \tag{2.23}$$

In these equations, $\alpha_{Ai}(i = x, z)$ is the phase lag between F_{Ii} and F_{Di}, and α_{Ii} $(i = x, z)$ is the phase lag between F_{Ii} and F_i. The second term in Eqs.(2.22) and (2.23) corresponds to the apparent drag force caused by the phase lag.

In the evaluation of the effect of the diffracted wave on the wave force, it is important to discuss the phase lag between F_{Ii} and F_{Di} as well as the magnitude of the wave force, since the phase lag decreases the wave force when it approaches π. Thus, in this study, the following coefficients, r_x and r_z, are introduced.

$$r_x = \frac{F_{DXm} \sin\alpha_{AX}}{F_{IXm} + F_{DXm} \cos\alpha_{AX}} \tag{2.24}$$

$$r_z = \frac{F_{DZm} \sin\alpha_{AZ}}{F_{IZm} + F_{DZm} \cos\alpha_{AZ}} \tag{2.25}$$

Using r_x and r_z, the total maximum forces and phase lags can be rewritten as follows:

$$Fx_m = (F_{IXm} + F_{DXm} \cos\alpha_{AX}) \sqrt{1 + r_x^2}\,, \quad \alpha_{IX} = \tan^{-1}(r_x) \tag{2.26}$$

$$Fz_m = (F_{IZm} + F_{DZm} \cos\alpha_{AZ}) \sqrt{1 + r_z^2}\,, \quad \alpha_{IZ} = \tan^{-1}(r_z) \tag{2.27}$$

For sufficiently small r_x and r_z, the magnitude of the total force is almost equal to the first term in Eqs.(2.26) and (2.27), which corresponds to the inertia term of the Morison equation, since the square values of r_x and r_z are much less than 1.0. On the other hand, large values of r_x and r_z mean that the wave diffraction plays a very important role on the wave force. Thus, in this study, the applicable range of the diffraction theory in the estimation of the wave force is judged from r_x and r_z. In the judgment, variations of the wave height are also taken into consideration.

Figures 2.5 and 2.6 show the variations of r_x and r_z with d/h and ka. In the figures, the line indicating $d = a + L/2$ is shown by the broken line. The fluid force acting on the sphere under the condition that $d > a + L/2$ is governed only by the hydrostatic pressure, since the water particle motion is quite small. Thus, the calculation was not performed under such conditions.

It was confirmed that the 5% wave height change corresponds to almost 3% change in r_x and r_z. Also, it was found that the wave diffraction takes place clearly when the r_x and r_z are larger than 3%. Therefore, the applicable range of the diffraction theory in evaluating the wave force is defined, in this study, as the range that r_x and r_z are larger than 3%. In the figures, this range is shown as the shaded area. As seen in the figures, the range in which the diffraction theory should be applied depends not only on the diffraction parameter, ka, but also on the relative diameter, D/h, and the relative submergence, d/h. Figures 2.5 and 2.6 also show that the effect of the diffracted wave on the wave force can be negligibly small even under a large diffraction parameter when the location of the sphere is sufficiently deep, since the water particle motion around the sphere is small. The effects of the diffracted wave on the

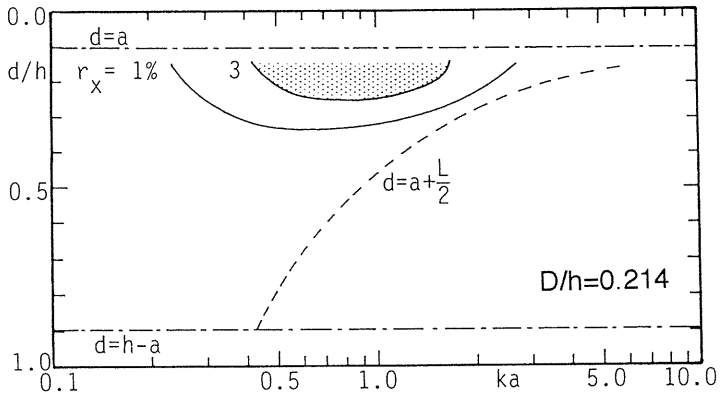

(a) D/h=0.214

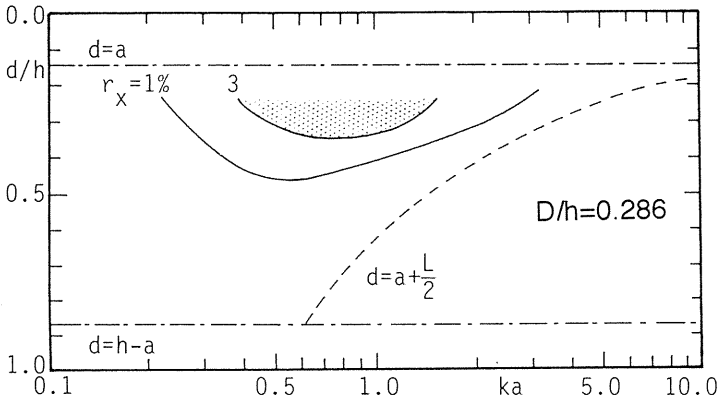

(b) D/h=0.286

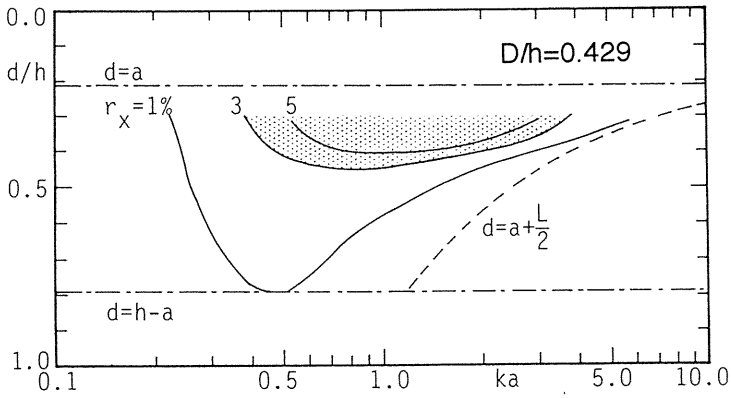

(c) D/h=0.429

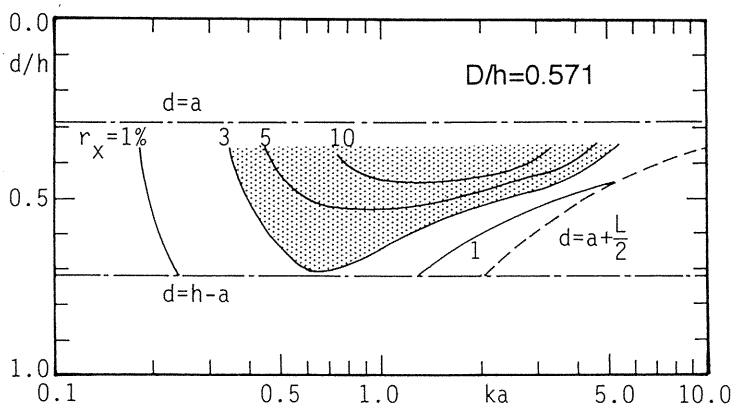

(d) D/h=0.571

Fig. 2.5 Dominating range of horizontal diffraction force (shaded area)

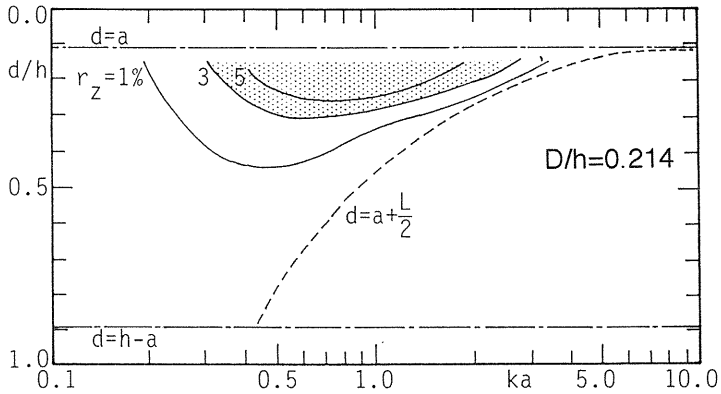

(a) D/h=0.214

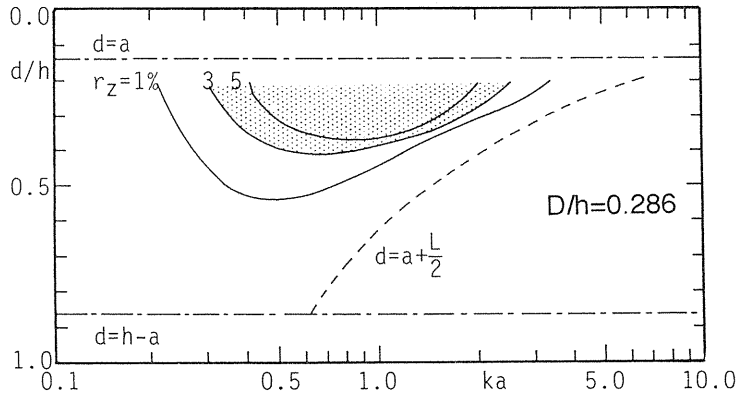

(b) D/h=0.286

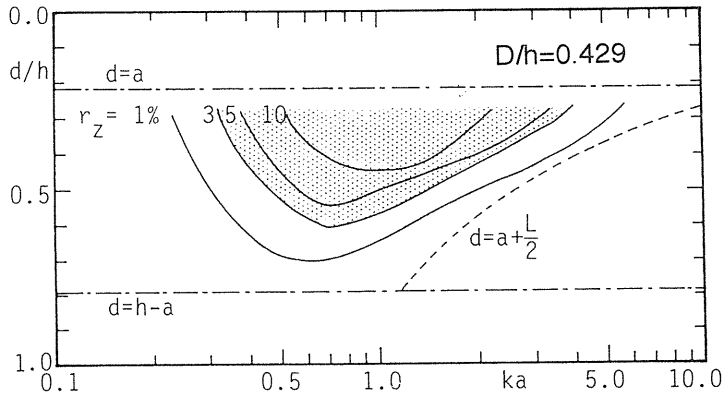

(c) D/h=0.429

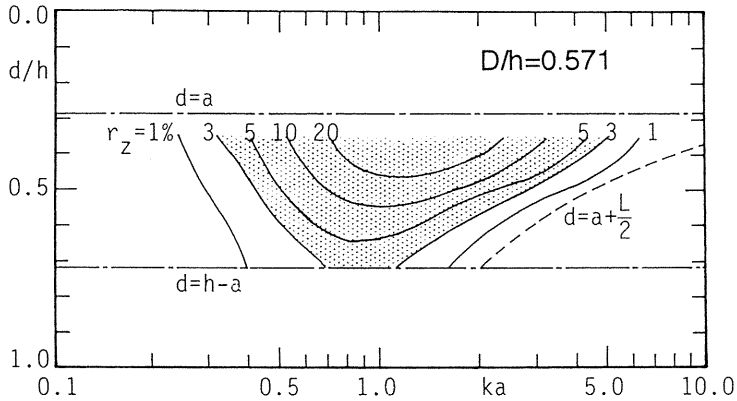

(d) D/h=0.571

Fig. 2.6 Dominating range of vertical diffraction force (shaded area)

wave force are revealed to be small when D/h is less than 0.14, while it has very significant effects on the wave force when D/h > 0.85 and ka > 0.3, although figures of which are not shown here.

2. 6 Effective Inertia Coefficient

In the previous section, the dominant range of the diffraction force is discussed. In this section, the characteristics of diffraction forces are discussed in terms of effective inertia coefficients C_{IX} and C_{IZ} defined by the Eqs.(2.28) and (2.29) are discussed.

$$C_{IX} = \frac{Fx_m}{\rho\pi D^3 \dot{u}_m/6} \tag{2.28}$$

$$C_{IZ} = \frac{Fz_m}{\rho\pi D^3 \dot{w}_m/6} \tag{2.29}$$

where, $\dot{u}$ and $\dot{w}$ are, respectively, the x- and z-directed water particle accelerations at the center of the sphere which are evaluated with the linear wave theory and subsuffix m indicates the maximum value. Figure 2.7 shows the relationship between C_{IX} and ka. In the figure, the curved line represents the calculated result by the SDM, in which the range of the broken line corresponds to the range where the wave diffraction significantly takes place and circles with horizontal bars indicate the values in the case that the wave breaking occurs.

Good agreements between the experimental and analytical results can be seen in these figures and no significant difference caused by the increasing wave height is recognized even under the condition that the wave breaking takes place. This indicates that the wave height has little effect on the effective inertia coefficient and the SDM based on the linear wave theory estimates accurately the experimental results which include results for nonlinear waves. The main reason why the wave breaking has little effect on C_{IX} is due to the facts that the breaker type observed in the experiment is the spilling-type breaker with small volume of

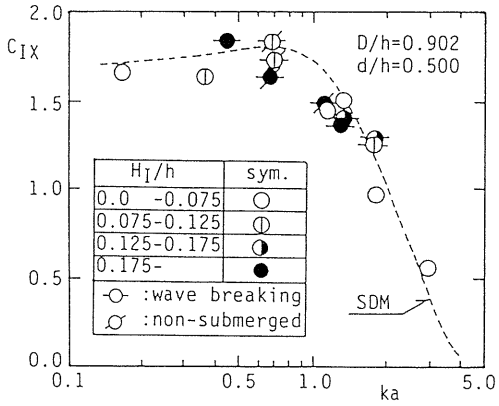

(a) D/h=0.902, d/h=0.50

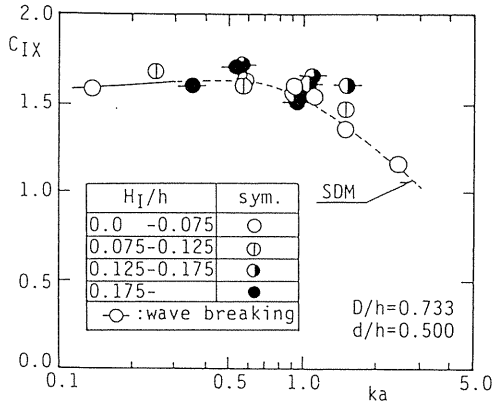

(b) D/h=0.733, d/h=0.50

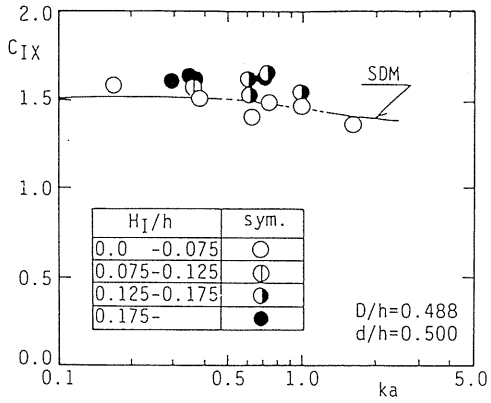

(c) D/h=0.488, d/h=0.50

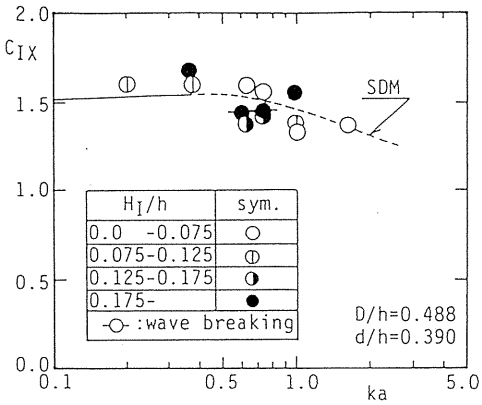

(d) D/h=0.488, d/h=0.39

Fig. 2.7 Relationship between C_{IX} and ka

the entrained air and that the disturbed water particle motion is only limited in the area near the free surface.

Effectiveness of present method based on the linear wave theory indicates that the diffraction force under irregular wave field can be evaluated by superposition of the result for each component wave.

As shown in Fig. 2.7, it was recognized as general tendencies that an increment of D/h enlarges the variation of C_{IX} with ka and that variation of C_{IX} with ka becomes remarkable with decreasing d/h. These results show that the relative diameter of the sphere, D/h and the relative submergence, d/h significantly affects the C_{IX}. The following reason can be applied to these facts. The sphere approaches the free surface with an increase of D/h and a decrease of d/h. This means that the water particle motion around the sphere becomes larger. Then, the wave is remarkably diffracted and the wave pressure on the sphere is largely fluctuated.

Variation of C_{IX} with ka becomes remarkable in the range that the diffraction theory should be applied in calculating the wave force (broken line in Fig. 2.7). On the contrary, C_{IX} can be regarded almost constant in the range that the effect of the wave diffraction on the wave force can be neglected (solid line). This indicates that the numerical calculations represent adequately the range in which the diffraction theory should be employed.

Figure 2.8 shows the relationship between C_{IZ} and ka. The fundamental properties of C_{IZ} are similar to those of C_{IX}. In other words, C_{IZ} varies evidently with ka in the range that wave diffraction becomes significantly. The contribution of D/h and d/h to C_{IZ} becomes larger than C_{IX}, and both D/h and d/h tend to affect more significantly C_{IZ} than C_{IX}. The variation of C_{IZ} with ka becomes large with an increment of D/h and decreasing of d/h, although the figure of which are not shown here. This would indicate that the free surface and bottom boundaries affect significantly the wave diffraction, and the vertical component of the wave pressure is more sensitively affected by the wave diffraction than the case of the horizontal pressure component.

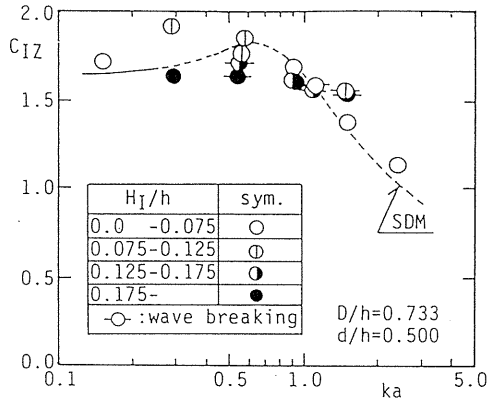

(a) D/h=0.733, d/h=0.50

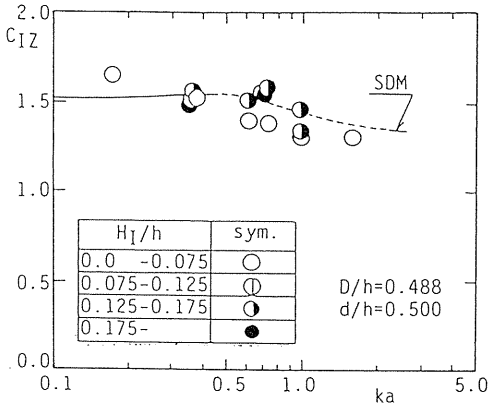

(b) D/h=0.488, d/h=0.50

Fig. 2.8 Relationship between C_{IZ} and ka

2. 7 *Conclusions*

In this chapter, the wave force acting on a submerged sphere with large diameter is discussed experimentally and theoretically. Conclusions obtained are summarized as follows:

1) The diffraction force on a submerged sphere is governed not only by the diffraction parameter ka but also by the relative submergence of the sphere d/h and the relative diameter D/h. The dimensionless wave height H_I/h, however, affects little the dimensionless wave force $Fx_m/\rho g H_I D^2$ and $Fz_m/\rho g H_I D^2$.
2) In the case that D/h is less than 0.9, the SDM is an effective and useful method in calculating the diffraction force on the sphere. In the range that D/h is more than 0.9, however, the SDM cannot be applicable to evaluate the vertical wave force acting on the submerged sphere, in which the wave run-up and run-down on the sphere affect the wave force.
3) The ranges in which the diffraction force should be taken into account are shown graphically, and the validity of these ranges are confirmed.

3. Wave Force Acting on a Submerged Sphere with Small Diameter

3. 1 Introduction

Existence of small objects does not affect the wave except for local disturbance. Thus, under such a condition, the diffraction force can be negligible, while the inertia, drag and lift forces are important for the estimation of acting wave force. These wave forces are closely related to the flow around objects. It is therefore important to reveal the wave-induced flow around the sphere. Jenkins and Inman[3)] observed the flow around the sphere and pointed out that the circulation streaming diminishes the wave pressure on the sphere. In their experiments, however, the location of the sphere was fixed and the effect of the submergence on the wave force and flow patterns was not discussed. This indicates that further investigation is necessary for in-depth understanding of the wave force.

The inertia and drag forces are categorized as the inline force which acts in the direction of water particle motion. These inline forces are more important than the lift force because of their large magnitude compared with the lift force, in general. The inline wave force on a small object is generally estimated by the Morison equation[12)], which expresses the wave force as a sum of the inertia and drag forces. In use of the Morison equation, the accurate estimation of the drag and inertia coefficients is necessary. Kono[2)] pointed out that the drag coefficient of the sphere in the wave field decreases with increasing Reynolds number (hereafter referred to as Re) and that the inertia coefficient can be approximated by 1.5. Jenkins and Inman[3)] obtained the similar result and stated that the drag coefficient decreases with increasing Keulegan-Carpenter number[13)] (hereafter referred to as KC). Both researches discussed only the horizontal wave force, and the vertical wave force was not investigated.

In the particular conditions, such as cases of a sphere located near the bottom or free surface boundaries and a case that strong vortex shedding takes place, the lift force plays an important part of the wave force as well as the drag and inertia forces. The Morison equation is not accurate enough to estimate such wave forces. It requires us to establish the new wave force formula which can evaluate well the wave force including the lift force.

With this background, this chapter is to investigate experimentally the wave force acting on a submerged sphere with small diameter.

3. 2 Experiments and Analysis

In the experiments, an indoor wave tank of 0.7 m in width, 0.95 m in depth and 25 m in length at Department of Civil Engineering, Nagoya University was used. Two kinds of experiments such as the wave force measurement and the flow visualization were carried out. In the experiments for the flow visualization, a horizontal step of 0.25 m height with a slope of 1/8 at the leading edge was installed. One part of the step was made of acrylate, and transparent and waterproofed camera box was set beneath the acrylic bed so as to enable to take flow pictures from a bed. The thin layered milk method using condensed milk was employed to visualize the wave-induced flow around the sphere. The wave-induced flows were taken pictures using synchronized two cameras with motor drive (5 frames/s) through the acrylic bed and a glass side wall of the wave tank. At the same time, the flows were also filmed with a high speed 16 mm cine-camera (50 frames/s) through the glass side wall. Details of the flow around the sphere were investigated with photographs and 16 mm films by means of a film motion analyzer. Asymmetry of the flow in the transverse direction to the wave propagation was discussed using the photographs taken from the bottom.

In the wave force measurements, the submergence of a sphere was changed finely near the bottom and free surface so as to investigate the boundary proximity effects. These

experimental conditions are summarized in Tables 3.1 and 3.2. For all experimental runs, the water surface elevation, the water particle velocities and the wave forces were simultaneously measured with a capacitance-type wave gauge, an electromagnetic-type velocimeter and cantilever-type wave force meters, respectively. Their time histories over 1 minute were recorded on magnetic tapes, and then they are digitized at a time interval of 0.05 s.

Table 3.1 Experimental conditions for flow visualization

h (cm)	45.0
h/gT^2	0.035, 0.020, 0.011
d/h	0.222, 0.356, 0.711, 0.889
D/h	0.141, 0.056, 0.021
u_mT/D	1.7 - 56

Table 3.2 Experimental conditions for wave force measurement

h (cm)	70.0
h/gT^2	0.054, 0.028, 0.022, 0.018, 0.014, 0.011
d/h	0.107 - 0.979
D/h	0.091, 0.036, 0.014
u_mT/D	0.4 - 100

3. 3 Flow Around a Submerged Sphere

The wave-induced flow pattern around the sphere is found to be classified into four types;

(a) Oscillating pattern without flow separation (Type-A)
(b) Oscillating pattern with flow separation (Type-B)
(c) Rotating pattern without flow separation (Type-C)
(d) Rotating pattern with flow separation (Type-D)

Schematic illustrations of time variations of the flow patterns over one wave period are shown in Fig. 3.1. In the figure, numbers in the left column mean the phases of the water surface profile in the top row.

The oscillating flow pattern is similar to that observed in the oscillatory flow[14]. In this pattern, the horizontal motion of the water particle dominates over the vertical one. When $KC_X(= u_mT/D)$ is small, water particles oscillate on the sphere without separation (Type-A). However, with increasing of KC_X, the excursion length of water particle becomes larger and then the flow separates (Type-B). The vortex ring is formed behind the sphere in every half cycle in the typical case of Type-B, as shown in Fig. 3.1(b).

The rotating flow pattern appears when the orbit of water particle is not so flat. For small KC_X, a vortex filament is formed on the sphere and it rotates around sphere (see Fig. 3.1(c)). As KC_X grows up, vortex filament becomes turbulent and flow separation takes place. The wake region rotates around the sphere in the typical case. Different from the oscillating flow pattern, no vortex ring is formed in the rotating flow pattern.

The occurrence of the rotating and oscillating flow patterns is largely governed by the ratio of the vertical excursion length of water particle to the horizontal one, γ $(=w_m/u_m)$, and the rotating flow pattern takes place for $\gamma > 1/2$ and the oscillating flow pattern occurs for $\gamma < 1/3$. In the range of $1/3 \leq \gamma \leq 1/2$ both flow patterns are observed. This means that the range of $1/3 \leq \gamma \leq 1/2$ is the transitional range from the oscillating flow pattern to the rotating one.

Next, let us consider the flow separation which has very significant effects on the maximum wave force. Figure 3.2 shows the relationship among the flow separation, KC_X and Re. Figure 3.2 indicates that when KC_X becomes large, the flow separation takes place. The

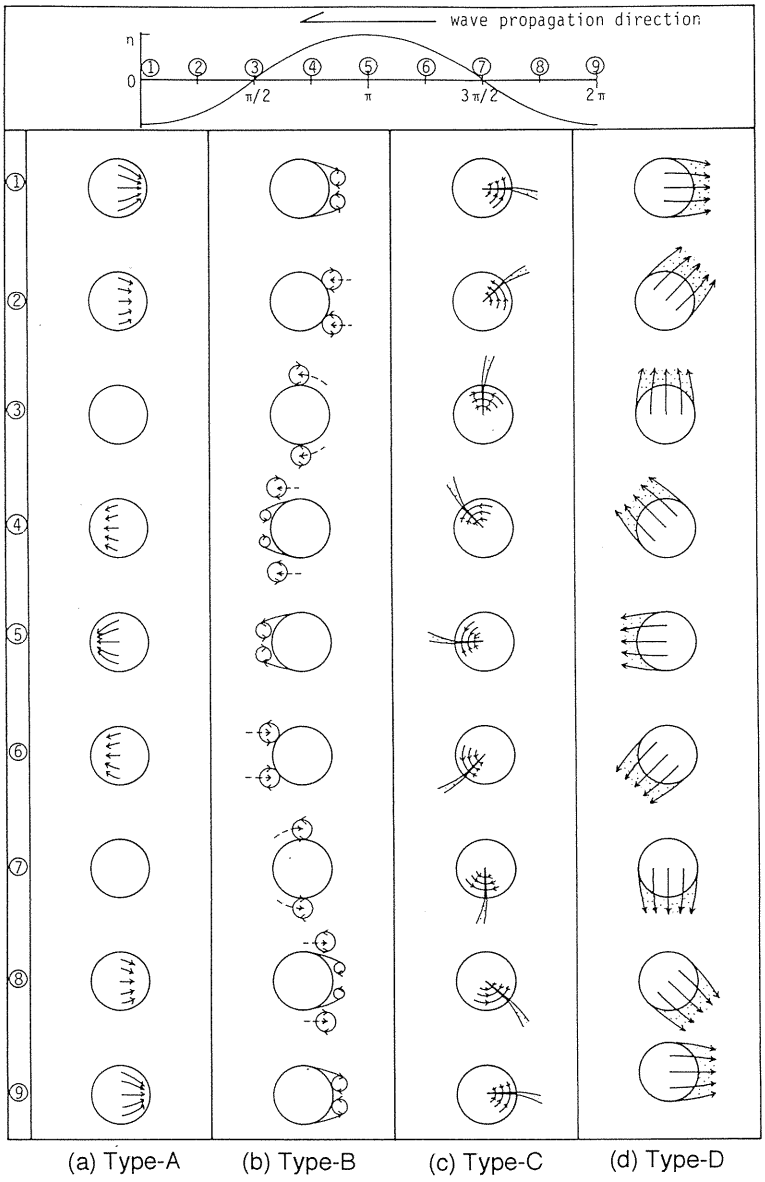

Fig. 3.1 Flow around a submerged shpere

smaller Re becomes, the larger the critical KC_X becomes. This criterion can be given by Eq.(3.1) in our experiments.

$$Re = 570000(KC_X)^{-3} \tag{3.1}$$

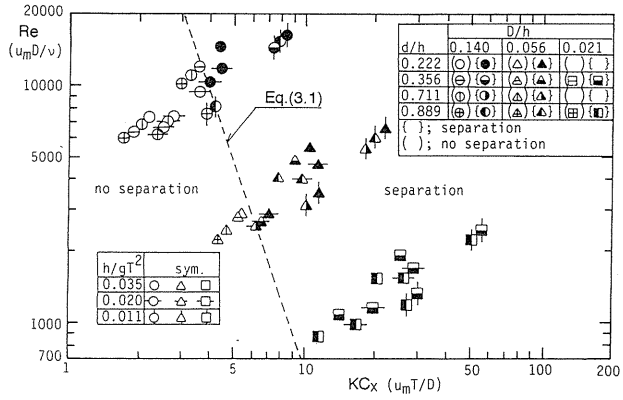

Fig. 3.2 Range of flow separation

Equation (3.1) indicates that the flow separates more easily as the effect of viscosity becomes smaller for a given KC_X.

3. 4 Applicable Range of Morison Equation

In the evaluation of the wave force on a small object, the Morison equation is usually applied. For Fx and Fz on a spherical body, the Morison equations are given as follows;

$$Fx = \frac{1}{8} C_{DX}\rho\pi D^2 u\sqrt{u^2 + w^2} + \frac{1}{6} C_{MX}\rho\pi D^3 \dot{u} \tag{3.2}$$

$$Fz = \frac{1}{8} C_{DZ}\rho\pi D^2 w\sqrt{u^2 + w^2} + \frac{1}{6} C_{MZ}\rho\pi D^3 \dot{w} \tag{3.3}$$

where C_{DX} and C_{DZ} are the drag coefficients, and C_{MX} and C_{MZ} are the inertia coefficients. In the Morison equation, only the drag and inertia forces are taken into account, and it is not applicable when the lift force is dominant wave force component. Thus, the applicable range of the Morison equation should be discussed. The correlation coefficient, r defined with Eq.(3.4) is employed to determine the applicable range:

$$r = \sqrt{1 - \overline{\{F_c(t) - F(t)\}^2}/\overline{F(t)^2}} \tag{3.4}$$

where, $F_c(t)$ and $F(t)$ are the calculated and measured wave forces, respectively, and superbar means the time average.

The Morison equation is judged, in this paper, to be applicable when r is larger than 0.9, since the difference between $F_c(t)$ and $F(t)$ is negligibly small for $r \geq 0.9$. The correlation coefficient r is calculated for all the experimental data. The values of r in the case of the horizontal wave force, Fx, are larger than 0.9 except for the case that the sphere does not emerge from the wave trough.

The correlation coefficients, r in the case of the vertical wave force, Fz are very scattered between 1.0 and 0.3 and applicable range of the Morison equation is very limited as shown in

Fig. 3.3. It can be seen that the Morison equation cannot be applied to evaluate the vertical wave force on the sphere near the free surface and bottom. In Fig. 3.3(a), the values of $\gamma=1/2$ and $1/3$ are simultaneously drawn as the dot-dash and broken curves, respectively. Synthesizing the inapplicable range and these curves, it is clear that the Morison equation cannot be applied when γ is less than $1/3$. In other words, the Morison equation is not applicable when the oscillating flow pattern is formed around the sphere. The applicable range of the Morison equation in other cases are given in Figs. 3.3(b) and (c).

The reason why the Morison equation cannot be applied may be mainly due to the horizontal velocity-induced lift force. That is, in the oscillating flow pattern, the horizontal motion of water particle dominates over the vertical one. Therefore the lift force due to the asymmetrical vortex shedding along the horizontal axis possibly becomes larger compared with the vertical drag and inertia forces. In addition, as d/h becomes larger, the horizontal velocities above and beneath the sphere differs largely due to the bottom proximity effect[15], and this asymmetry of the velocities causes the vertical drift and second harmonic forces even in the unseparated flow.

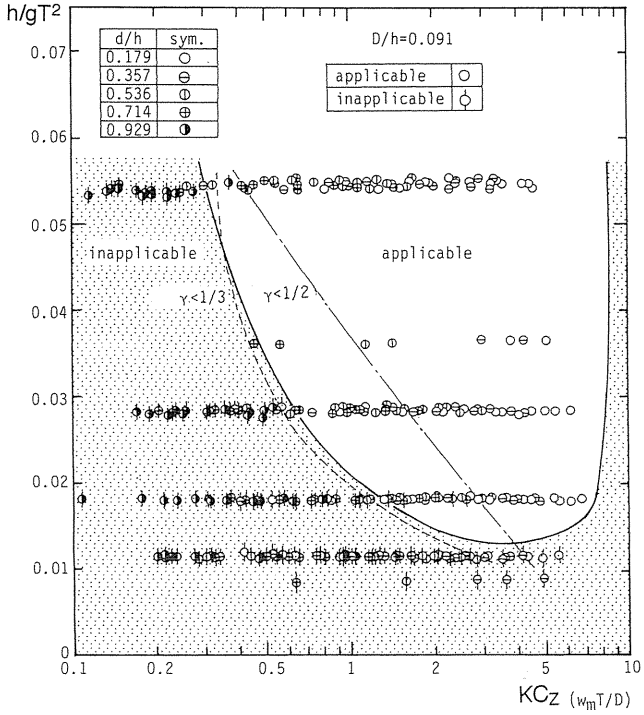

(a) D/h=0.091

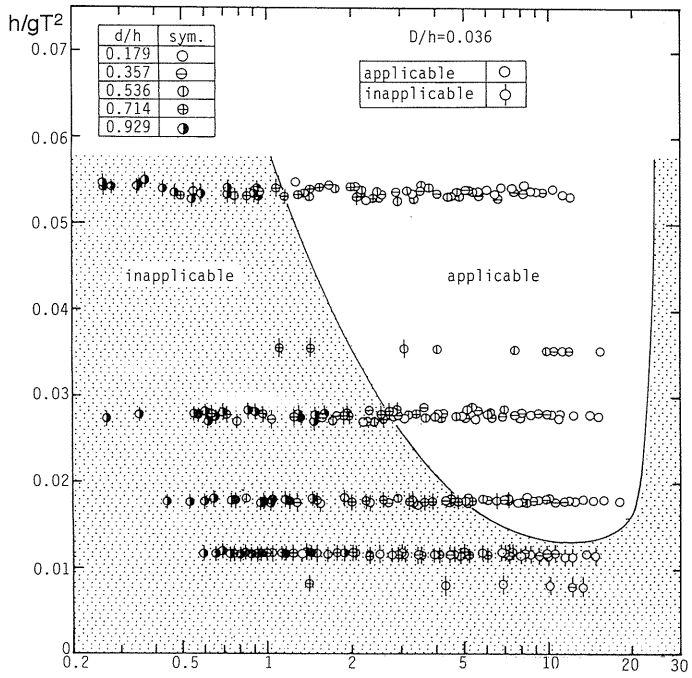

(b) D/h=0.0036

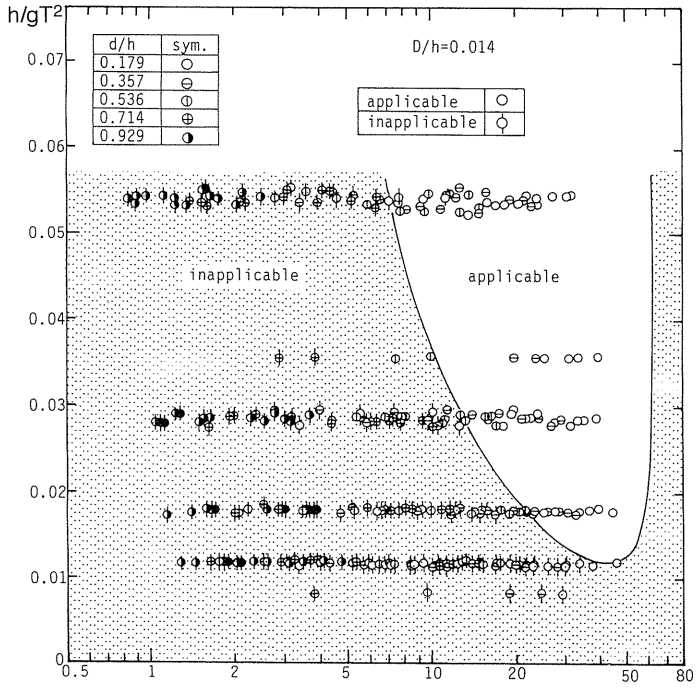

(c) D/h=0.014

Fig. 3.3 Applicable range of the Morison equation

3. 5 Inertia Coefficient

We discuss here the force coefficients in the applicable range of the Morison equation. Figure 3.4 shows the relationship between C_{MX} and KC_X. For KC_X smaller than 10, C_{MX} can be regarded as almost constant and no significant contributions of h/gT^2, d/h and D/h are recognized. On the other hand, in the range of $KC_X > 10$, C_{MX} decreases a little with increasing KC_X and it takes a minimal value at KC_X around 20, and then increases with an increment of KC_X. The minimal value becomes smaller with decreasing of d/h. It is clear that C_{MX} varies with KC_X when KC_X is larger than 10. The flow separation takes place in almost all cases when KC_X is larger than 10, and the pressure distribution on the sphere due to separated flow differs from that of the unseparated flow. This difference may characterize C_{MX} and the magnitude of C_{MX} is thought to be controlled by KC_X. Comparing our experimental data with the others' values measured in the oscillatory flow field[14),16)], there are no large discrepancies among them in the range of $5 < KC_X < 20$.

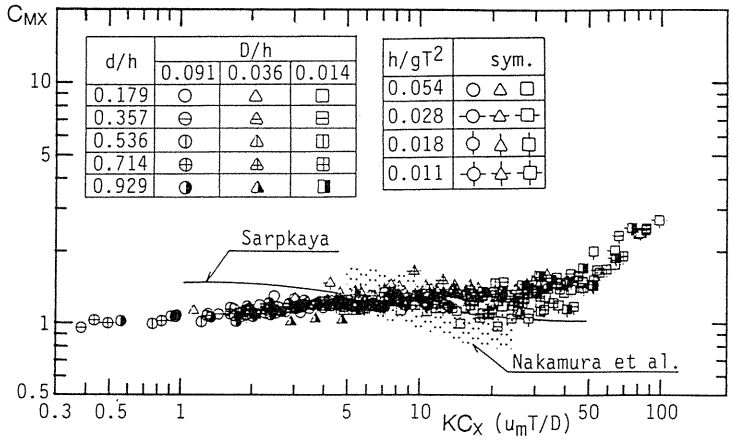

Fig. 3.4 Relationship between C_{MX} and KC_X

Relationship between C_{MZ} and $KC_Z(= w/_mT/D)$ is given in Fig. 3.5. Figure 3.5 indicates that variations of C_{MZ} with KC_Z are generally similar to those of C_{MX}, in the range of $KC_Z < 30$. Different from C_{MX}, the values of C_{MZ} vary with h/gT^2 as well as d/h, and it seems that the minimal value decreases with decreasing of h/gT^2. This would suggest that the lift force plays an important role in causing the difference between C_{MX} and C_{MZ}.

Our experimental data of C_{MX} and C_{MZ} are scattered a little. However, the mean values of these can be well formulated graphically with the function of the dominating parameters, and they are given in Figs. 3.6 and 3.7.

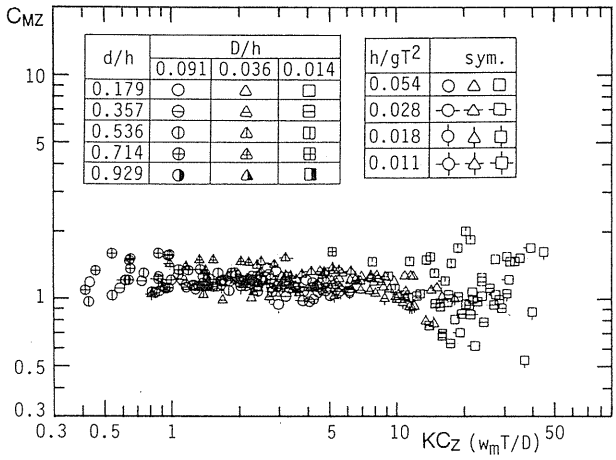

Fig. 3.5 Relationship between C_{MZ} and KC_Z

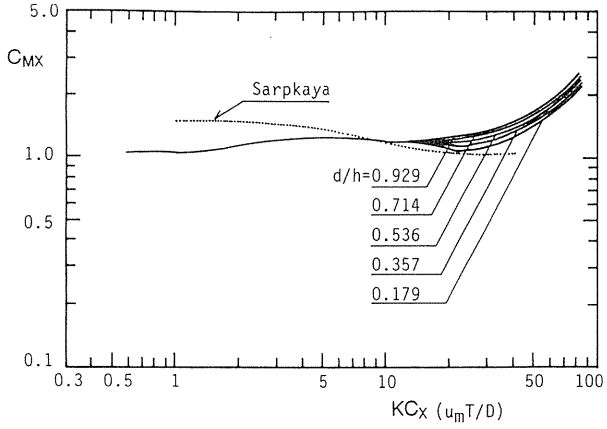

Fig. 3.6 Mean values of C_{MX}

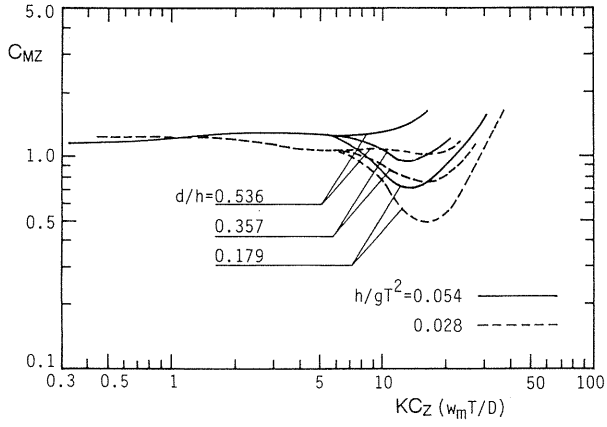

Fig. 3.7 Mean values of C_{MZ}

3. 6 Drag Coefficient

Figure 3.8 shows the relationship between C_{DX} and KC_X, in which the values in the oscillatory flow experiments[14),16)] are also drawn for comparison. When KC_X is less than 5 and the inertia force largely dominates over the drag force, the drag coefficients are very scattered and they are not plotted in the figure. It is seen that C_{DX} is affected by h/gT^2 and d/h in the range of KC_X up to 10. In the case of $h/gT^2=0.011$, C_{DX} decreases with increasing KC_X. On the contrary, C_{DX} increases with an increment of KC_X in the cases of $h/gT^2>0.018$. In addition, the smaller h/gT^2 is and the larger d/h is, the larger C_{DX} becomes. When KC_X is smaller than 10, the effect of the flow separation is not so large as already mentioned, and the friction due to the viscosity which depends on the velocity distribution on the sphere is main component of the drag force. The velocity distribution on the sphere changes with the flow pattern characterized by h/gT^2 and d/h. Therefore, the drag coefficient is governed by h/gT^2 and d/h when KC_X is smaller than 10.

The drag coefficient, in the range that KC_X is larger than 10, is almost constant and no significant change due to h/gT^2 and d/h is recognized. In this range, the flow separation occurs in almost all cases, and asymmetric pressure distribution due to the flow separation becomes a leading factor of the drag force in place of the friction. Although the difference in the vortex ring formation is recognized between the oscillating and rotating patterns, it can be said that the difference in the asymmetry of the pressure distribution between the two flow patterns has little effect to the drag coefficient in the range of $KC_X>10$.

Relationship between C_{DZ} and KC_Z is given in Fig. 3.9. Different from C_{DX}, C_{DZ} in the range that KC_Z is larger than 10 varies with h/gT^2. This may be largely due to the horizontal velocity-induced lift force. Except for that, general tendency of C_{DZ} is similar to C_{DX}.

The mean values of C_{DX} and C_{DZ} can be well formulated graphically as the functions of KC and h/gT^2, and they are given in Figs. 3.10 and 3.11, respectively. Although C_{DX} and C_{DZ} are also affected by d/h, its contribution is very small compared with that of h/gT^2. Then the effect of d/h is implicitly included in the formulated curves. Using the drag coefficients given in Figs. 3.10 and 3.11 and the inertia coefficients in Figs. 3.6 and 3.7, the wave force acting on a submerged sphere can be evaluated with high accuracy in the applicable range of the Morison equation.

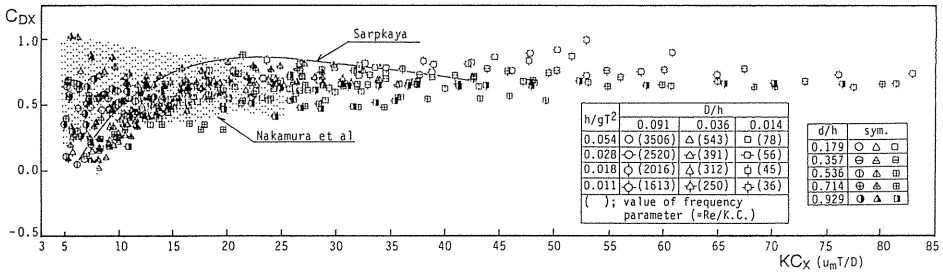

Fig. 3.8 Relationship between C_{DX} and KC_X

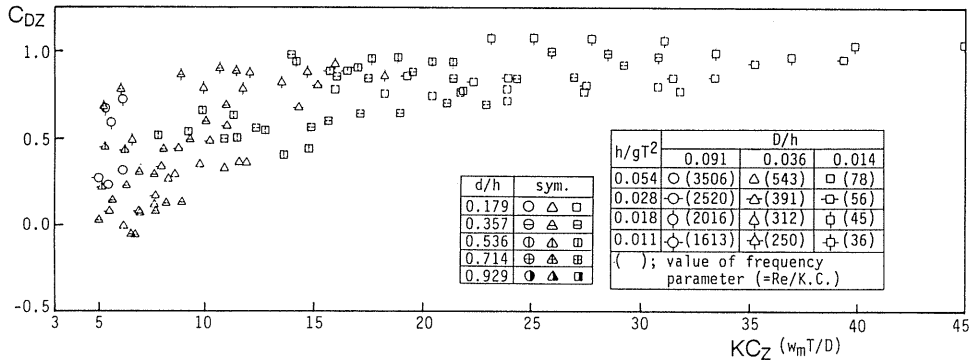

Fig. 3.9 Relationship between C_{DZ} and KC_Z

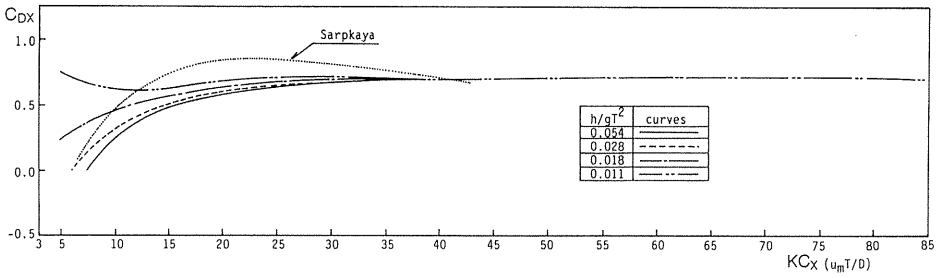

Fig. 3.10 Mean values of C_{DX}

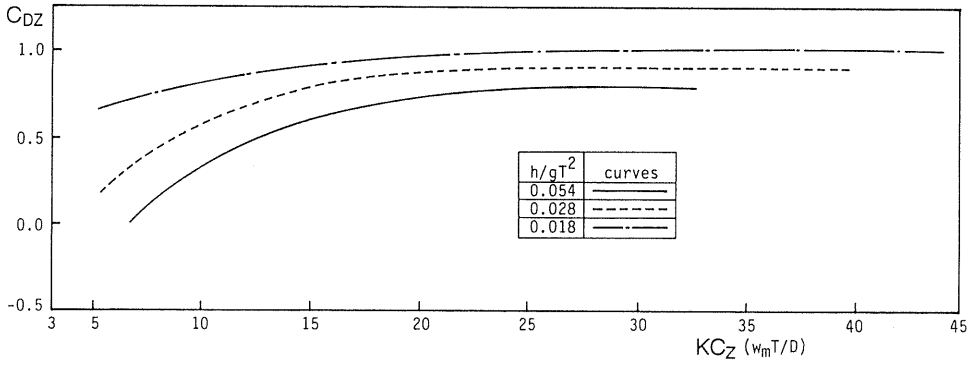

Fig. 3.11 Mean values of C_{DZ}

3. 7 Maximum Wave Force

Figure 3.12 shows a relationship between the non-dimensional maximum force in x-direction, Fx^* ($=Fx_m/\rho(u\sqrt{u^2+w^2})_m D^2$) and KC_X, in which the maximum and minimum values of KC_X which the flow separation takes place are indicated. The followings can be pointed out from this figure. The dimensionless maximum wave force in the unseparated flow field is proportional to $(KC_X)^{-1}$. This means that the maximum wave force is proportional to the wave height. In the range of $4 < KC_X < 11$, the flow around the sphere separates in some cases, and the decreasing rate of Fx^* with KC_X becomes gentle. The flow separates in all cases in the range that KC_X is larger than 11, and Fx^* approaches to a constant value. This implies that the maximum wave force is proportional to the squared wave height. Thus, it is clear that the maximum wave force is remarkably subjected to whether the flow is separated or not.

The non-dimensional inertia and drag forces calculated with $C_{MX}=1.2$ and $C_{DX}=0.7$, respectively, are also shown in Fig. 3.12. Here, $C_{MX}=1.2$ is the averaged value of C_{MX} in the range of $KC_X < 10$, in Fig. 3.6, and $C_{DX}=0.7$ is also the averaged value of C_{DX} in the range of $KC_X > 10$, in Fig. 3.10. The good agreement between the calculated inertia force and experimental values in the range of $KC_X < 10$ is recognized. Also, the calculated drag force agrees well with experimental values in the range of $KC_X > 10$. The similar result is obtained in the case of the z-directed wave force, as shown in Fig. 3.13.

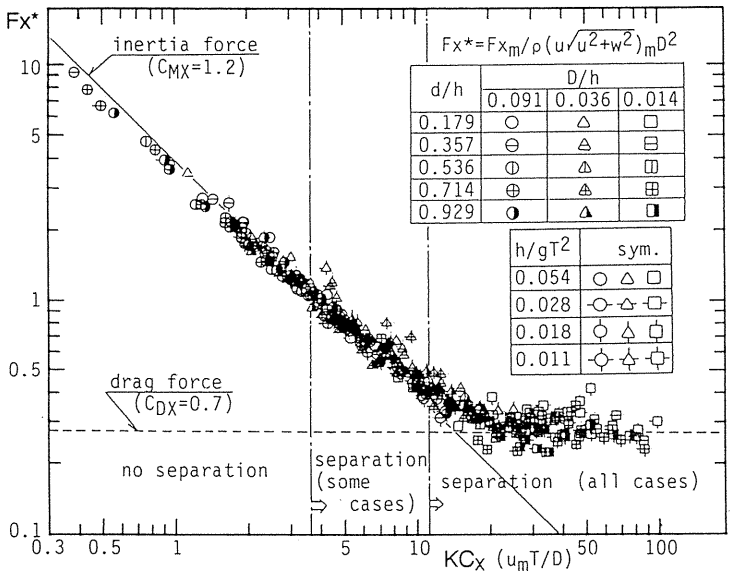

Fig. 3.12 Relationship between Fx^* and KC_X

These results suggest that the wave force can be evaluated with only the inertia force when the inertia force dominates over the drag force. In this case, the Morison equation can be simplified as

$$Fx = \frac{1}{6} C_{MX}\rho\pi D^3 \dot{u} \tag{3.5}$$

$$Fz = \frac{1}{6} C_{MZ} \rho \pi D^3 \dot{w} \tag{3.6}$$

Conversely, the wave force can be estimated with the following simplified equations in the case that the drag force dominates over the inertia force.

$$Fx = \frac{1}{8} C_{DX} \rho \pi D^2 u \sqrt{u^2 + w^2} \tag{3.7}$$

$$Fz = \frac{1}{8} C_{DZ} \rho \pi D^2 w \sqrt{u^2 + w^2} \tag{3.8}$$

The applicability of these wave force formulae will be discussed in Section 3.10.

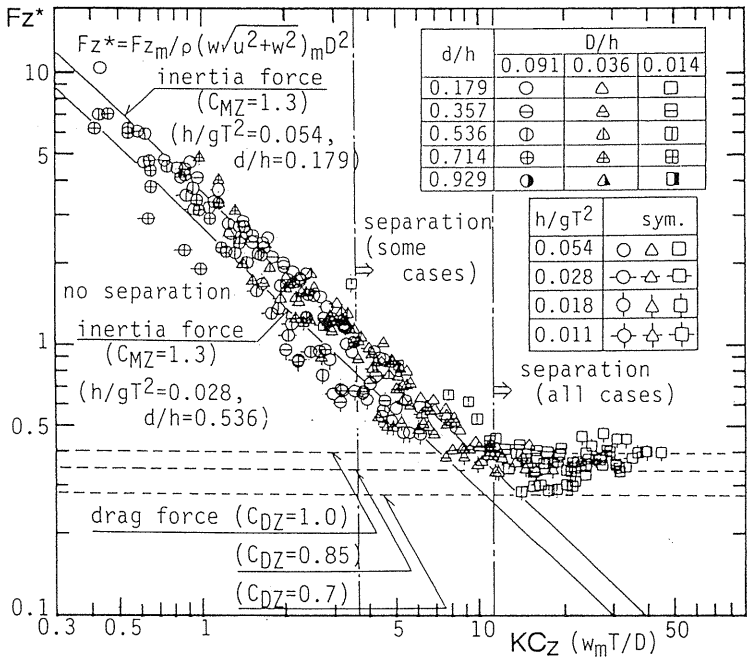

Fig. 3.13 Relationship between Fz* and KC_Z

3. 8 Boundary Proximity Effects

Boundary proximity is very important factor for the wave force acting on a sphere, in particular on the vertical wave force, when it is located near the bottom or free surface boundaries. The effects of these boundaries, however, are different each other because the bottom is a fixed boundary, whereas the free surface is moving one. Thus, in this section, proximity effects of these boundaries on vertical wave force are discussed separately.

3. 8. 1 Bottom Boundary Proximity

(1) Time Profile

In this case, the time variations of the vertical wave forces can be classified largely into three types, such as S-type, T-type and R-type, as shown in Fig. 3.14. S-type profile has one pair of regular maximal and minimal values in one wave period, while T-type profile has two pairs. This type can be further divided into two types such as T-1 and T-2-types, as shown in Fig. 3.14(b) and (c). T-1-type has a regular profile and quite similar variations are repeated. On the other hand, T-2-type profile has different maximal and minimal values. R-type profile does not show regular peak values. In all the cases, both water surface and water particle velocity profiles are sinusoidal.

The appearance of these profiles is affected by KC_X, D/h and γ which is correlated with h/gT^2 and d/h. S-type wave force can take place mainly in the case that KC_X is less than 4. In this range, the flow separation does not occur and the inertia force dominates over the drag one. Moreover, the excursion length of water particle motion is smaller than the sphere diameter and then the nonlinear effect which causes the second harmonic wave force is not large. This would suggest that this type of the wave force is little affected by the bottom proximity.

T-1-type wave force was observed only in the limited range of D/h=0.091 and $4 < KC_X < 8$. Considering that this time variation is regular and the effect of the flow separation to the wave force is small in that range, the T-1-type wave force may be strongly affected by the lift force caused by the asymmetric pressure distribution due to the accelerated velocity below the sphere. T-2-type wave force was observed for the larger value of KC_X than that of the T-1-type. Judging from its irregular variation, the lift force caused by the asymmetric vortex formation and viscous drag may play important roles.

R-type wave force takes place mainly under the flow condition of large KC_X and is thought to be caused by the vortex shedding or disturbance of the flow along the sphere surface. T-2-type and R-type profiles are apt to appear more frequently as D/h decreases. This can be due to the fact that the flow around the sphere tends to be strongly turbulent as D/h becomes smaller[17].

(2) New Formula to Evaluate the Wave Force

The Morison equation can be applied to the S-type wave force. However, there is no formula to evaluate other type wave forces. T-1-type wave force is characterized by the second harmonic component and steady one whose direction is downwards, as shown in Fig. 3.14(b). Near the bottom boundary, the horizontal component of water particle velocity dominates over the vertical one and the lift force caused by the horizontal component of water particle velocity plays an important role. The vertical lift force acting on a sphere in the horizontal flow field can be approximated as following form by extending the potential theory derived by Lamb[18].

$$Fz = -\frac{1}{6}\rho\pi D^3 C_1 u^2, \quad C_1 = \frac{9D^3}{512e_1^4} \tag{3.9}$$

where e_1 is the distance from sphere center to the bottom.

The lift force given by Eq.(3.9) is composed of the steady and second harmonic components and both components increase as the sphere approaches to the bottom. Figure 3.15 shows the variation of the ratio of the steady component to the total wave force Fz_0/Fz_m with e_1/D under the condition of h/gT^2=0.018. In the figure, the calculated value with Eq.(3.9)

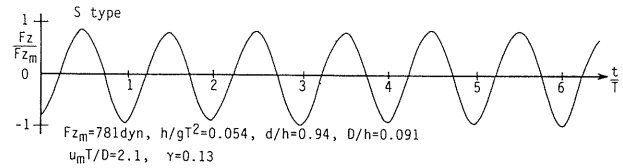

(a) S-type

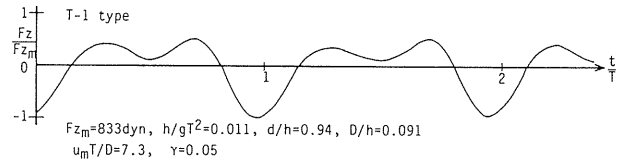

(b) T-1-type

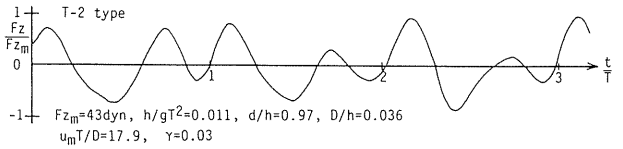

(c) T-2-type

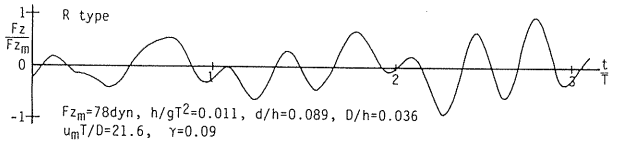

(d) R-type

Fig. 3.14 Time profiles of vertical wave forces (near bottom boundary)

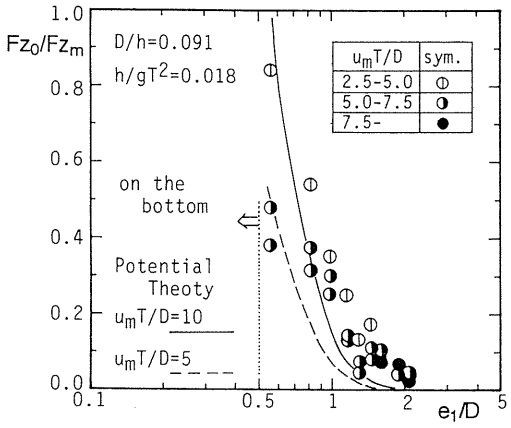

Fig. 3.15 Variation of Fz_0/Fz_m with e_1/D

are also shown for comparison. Experimental results show that the contribution of the steady component wave force to the total wave force is very small in the range of $e_1/D > 1.5$, but it becomes remarkably larger with decreasing e_1/D in the range of $e_1/D < 1.5$. These tendencies agree well with the calculated values based on the potential theory, as shown in Fig. 3.15. The similar result is obtained for the second harmonic component force. These facts indicate that the wave force component presented in Eq.(3.9) is possibly included in the wave force acting on the sphere located near the bottom, although Eq.(3.9) does not satisfy the boundary condition completely. Therefore, it is appropriate to consider that the T-1-type wave force can be expressed by adding Eq.(3.9) to the Morison equation, Eq.(3.3). This paper proposes here Eq.(3.10) as a new formula to evaluate the T-1-type wave force.

$$\begin{aligned} Fz = & \frac{1}{8} C_{DZ}\rho\pi D^2 w\sqrt{u^2 + w^2} + \frac{1}{6} C_{MZ}\rho\pi D^3 \dot{w} \\ & + \frac{1}{6} C_{L1}\pi\rho D^3 C_1 \overline{u^2} + \frac{1}{6} C_{L2}\rho\pi D^3 \left(u^2 - \overline{u^2}\right) \end{aligned} \tag{3.10}$$

In Eq.(3.10), the force expressed by Eq.(3.9) is decomposed into two terms which are proportional to the steady and second harmonic components, and C_{L1} and C_{L2} are, respectively, the corresponding lift coefficients introduced to adjust the effect of the boundary condition and contribution of the vertical component of water particle velocity to the wave force. In the case that the drag force is neglected, the following equation is derived from Eq.(3.10).

$$Fz = \frac{1}{6} C_{MZ}\rho\pi D^3 \dot{w} + \frac{1}{6} C_{L1}\rho\pi D^3 C_1 \overline{u^2} + \frac{1}{6} C_{L2}\rho\pi D^3 C_1 \left(u^2 - \overline{u^2}\right) \tag{3.11}$$

Comparisons between the measured and calculated wave forces are shown in Fig. 3.16. Three calculation methods such as Method-1, Method-2 and Method-3 stated below are employed to estimate the time variation of wave force.

- Method-1: This method uses Eq.(3.10). All the force coefficients (C_{DZ}, C_{MZ}, C_{L1} and C_{L2}) are determined by the least square method.
- Method-2: This method uses Eq.(3.10). The formulated drag and inertia coefficients (C_{DZ} and C_{MZ}) for the applicable range of the Morison equation are employed, whereas the lift coefficients (C_{L1} and C_{L2}) are determined by the least square method.
- Method-3: This method uses Eq.(3.11). The formulated inertia coefficient (C_{MZ}) is employed, and the lift coefficients (C_{L1} and C_{L2}) are determined by the least square method.

It is clear from Fig. 3.16 that the calculated values by means of Method-1 (thin solid line) agree well with the measured one (heavy solid line), and validity of the proposed formula Eq.(3.10) can be recognized. Equation (3.10) is found to be applicable to the sphere of $D/h=0.091$ under condition that $0.5 < e_1/D < 1.5$ and KC_X is approximately from 4 to 10. Figure 3.16 also shows that Eq.(3.11) can be also applied from practical engineering viewpoint. The applicable range of which will be discussed in Section 3.10.

For four coefficients in Eq.(3.10), following results are obtained. The value of C_{MZ} is confirmed to be close to the formulated values for the applicable range of the Morison equation[19]. Regarding the drag coefficient C_{DZ}, they are widely scattered, however, this type of wave force appears only when KC_Z is less than 10 and the drag force is dominated by the inertia force, thus, the contribution of the scattered drag coefficient to the total wave force is very small. Moreover, the term of the drag force can be neglected without lacking accuracy. Figures 3.17 and 3.18 show the relationships between C_{L1} and e_1/D and between C_{L2} and

e_1/D, respectively. C_{L1} and C_{L2} increase with an increment of e_1/D. Although the values are scattered a little, the mean values of C_{L1} and C_{L2} can be formulated as follows.

$$C_{L1} = a(e_1/D)^2 \tag{3.12}$$

$$C_{L2} = b(e_1/D)^2 \tag{3.13}$$

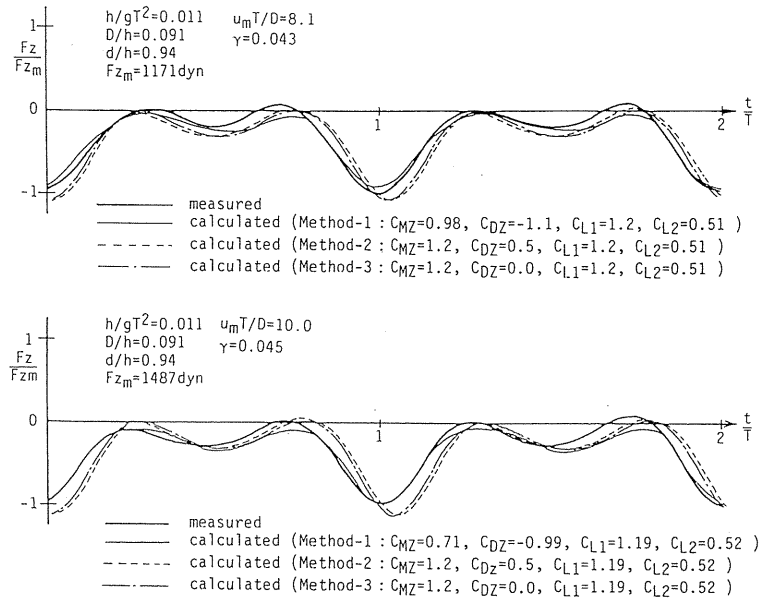

Fig. 3.16 Comparisons between measured and calculated wave forces

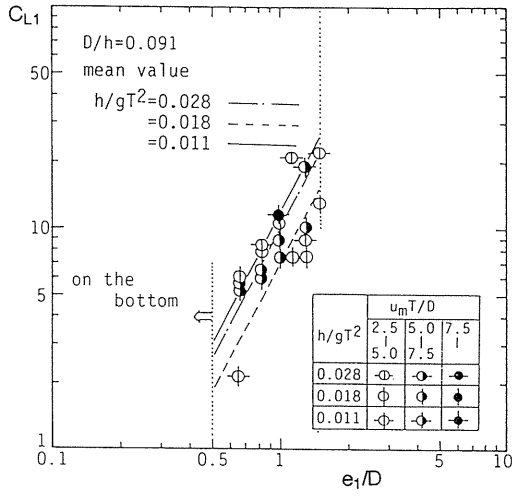

Fig. 3.17 Relationship between C_{L1} and e_1/D

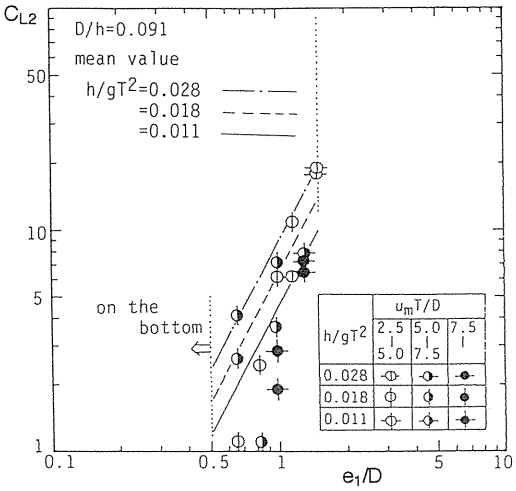

Fig. 3.18 Relationship between C_{L2} and e_1/D

where a and b are the coefficients taking a=10.1 and b=8.3 for h/gT^2=0.028, a=11.6 and b=6.2 for h/gT^2=0.018 and a=6.8 and b=4.4 for h/gT^2=0.028.

Concerning the T-2 and R-type wave forces, it is hard to propose an estimation formula, since the wave forces are strongly affected by the vortex formation and shedding and their mathematical modeling is very difficult. Treatment such wave forces will be discussed in Section 3.9.

3. 8. 2 Free Surface Proximity

(1) Time Profile

Time profile of the vertical wave force on a sphere located near the free surface can be classified into two types, such as S-type and T-type. Figure 3.19 shows the time variations of

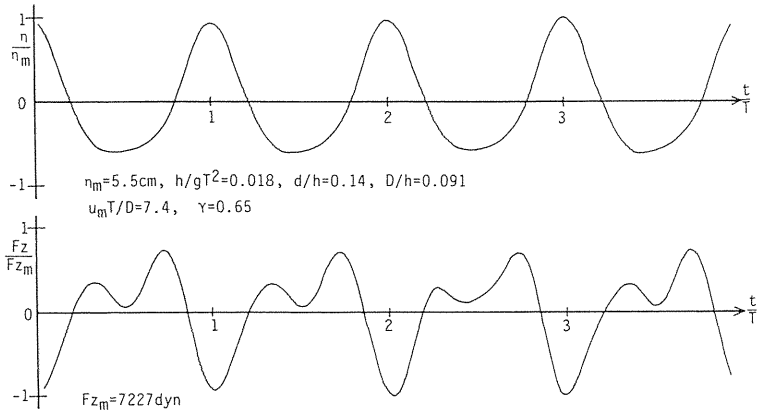

Fig. 3.19 Time profiles of surface elevation and vertical wave force (near free surface)

the water surface elevation and T-type vertical wave force. T-type wave force has a minimal value at the phase of the wave trough. Based on the visual investigation, the disturbance was observed on the free surface when the free surface approaches the sphere. This would suggest that the T-type profile is caused by the lift force due to the free surface proximity. On the other hand, S-type wave force is dominated by the drag and inertia forces rather than the lift force caused by the free surface proximity, and therefore the free surface proximity may not be important so much to this type wave force.

The appearance range of both types are almost defined by KC_Z, e_2/D (e_2 : distance from sphere center to wave trough) and γ, as shown in Fig. 3.20. T-type wave force is apt to appear as e_2/D decreases and it hardly occurs in the case that $e_2/D > 5.0$. When γ is larger than 0.7, T-type wave force is not observed even for the case that e_2/D is less than 5.0. This may be due to the following reason. That is, the vertical particle motion becomes larger with an increment of γ and the vertical drag and inertia forces become dominant over the lift force caused by the free surface proximity. In particular, T-type profile is not observed for a small sphere (D/h=0.014), for which KC_Z is larger than 20 and the vertical drag force is much larger than the inertia and the lift forces caused by the proximity effect. From this result, the free surface proximity effect on the wave force may be negligibly small for the condition that KC_Z is larger than 20.

As shown in Fig. 3.19, the downward force acts on the sphere at the phase of wave trough due to the water surface proximity. Therefore, in the case that the inertia force dominates over the drag force, the lift force diminishes the positive maximum vertical wave force. On the other hand, in the case that the drag force is predominant over the inertia one, the free surface proximity affects little the maximum vertical wave force, since the lift force acts at the phase of wave trough at which the vertical velocity is zero. Therefore, the absolute value of the maximum vertical force is hardly affected by the free surface proximity.

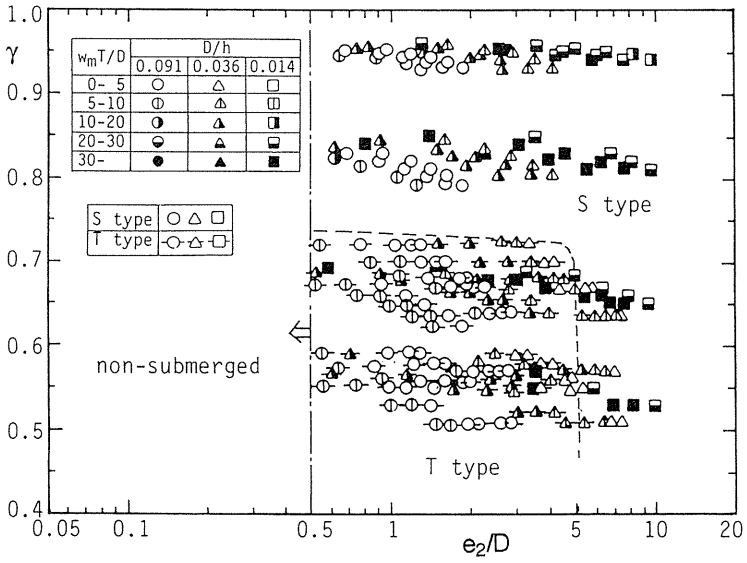

Fig. 3.20 Appearance range of S-type and T-type wave forces

(2) Characteristics of T-type Wave Force

The spectrum analysis has revealed that T-type wave force are mainly composed of the fundamental and second harmonic components[20]. The fundamental harmonic component force is closely correlated with the drag and inertia force and the second harmonic component is controlled by the lift force caused by the free surface proximity.

Figure 3.21 shows the variation of the amplitude of the second harmonic component normalized by the buoyancy of the sphere, Fz_2^*, with e_2/D. Fz_2^* tends to increase with decreasing of D/h and h/gT^2, and Fz_2^* decreases as e_2/D increases for given values of D/h, h/gT^2 and d/h. From these results, the following relationship can be derived.

$$Fz_2^* \propto (e_2/D)^{-3} \tag{3.14}$$

The relationship between Fz_2^* and KC_X is shown in Fig. 3.22. Fz_2^* becomes larger with

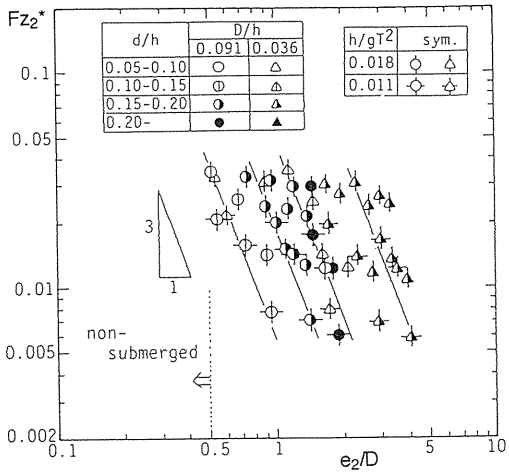

Fig. 3.21 Relationship between Fz_2^* and e_2/D

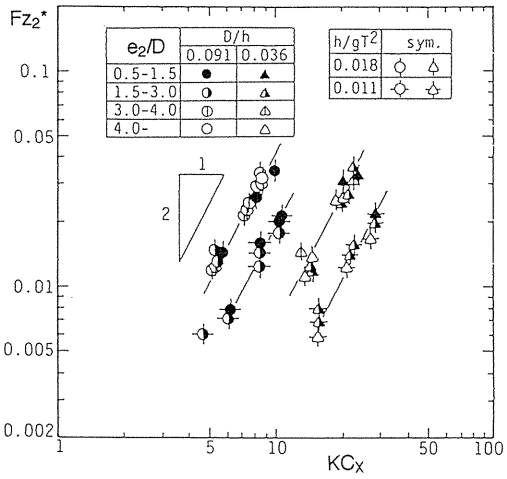

Fig. 3.22 Relationship between Fz_2^* and KC_X

increasing KC_X for given D/h and e_2/D, and it can be seen that the $Fz_2{}^*$ is proportional to u^2 as shown by the solid lines, which leads to the following relationship.

$$Fz_2{}^* \propto u^2 \tag{3.15}$$

(3) New Formula to Evaluate T-type Wave Force

Kim[21] discussed the effect of the existence of the free surface to the force acting on a sphere in an uniform flow field and pointed out that the lift force exerts on the sphere due to the interaction between the sphere and the free surface. He showed that the lift force is proportional to $(e_2/D)^{-3}$ and u^2 in his first order solution. The results obtained in this study are very close to his results. Although his result is only applicable to the uni-directional flow field, it can be assumed that the similar phenomena occur in the wave field, since the water particle motion is only horizontal at the phase of wave trough. It is therefore reasonable to employ his relationships to build a new formula to evaluate the T-type vertical wave force affected by the free surface proximity. This paper proposes Eq.(3.16) as a new formula to evaluate the T-type wave force.

$$Fz = \frac{1}{8} C_{DZ}\rho\pi D^2 w\sqrt{u^2 + w^2} + \frac{1}{6} C_{MZ}\rho\pi D^3 \dot{w} + \frac{1}{32} C_{L3}\rho\pi D^2 u^2 \left(\frac{D}{\eta + d}\right)^3 \tag{3.16}$$

where, C_{L3} is the lift coefficient. In the equation, the third term of the right hand side represents the lift force caused by the proximity of the free surface. $(\eta+d)$ is adopted instead of e_2 so as to introduce the time variation of distance between the sphere and the free surface. The calculated wave force is compared with the measured one in Fig. 3.23, in which the force coefficients are determined by the least squares method. It can be said that the agreement between measurements and calculations is very good, although some minor discrepancy is recognized at the phase of wave trough. Equation (3.16) is found to be applicable to the wave force under the conditions that $h/gT^2 < 0.022$ and $0.5 < e_2/D < 5.0$ (approximately corresponding to $\gamma < 0.7$), and that the drag force does not dominates[19].

If the drag force is negligibly small, Eq.(3.16) can be simplified as

$$Fz = \frac{1}{6} C_{MZ}\rho\pi D^3 \dot{w} + \frac{1}{32} C_{L3}\rho\pi D^2 u^2 \left(\frac{D}{\eta + d}\right)^3 \tag{3.17}$$

Applicability of this equation will be discussed in Section 3.10.

(4) Coefficients in the Formula

The relationship between C_{MZ} and KC_Z is shown in Fig. 3.24, in which the formulated value of C_{MZ} for the applicable range of the Morison equation is also shown as a solid line. Although the experimental condition is different a little, the inertia coefficient obtained in the present study corresponds well with the solid line. Figure 3.25 shows the relationship between C_{DZ} and KC_Z, in which the solid lines are the formulated values for the applicable range of the Morison equation for h/gT^2=0.018. The present experimental results for h/gT^2=0.018 agree well with the solid line. Because of lack of the data in the applicable range of the Morison equation for h/gT^2=0.022 and 0.011, further detailed discussion cannot be done.

However, C_{DZ} for h/gT^2=0.022 are also close to those for h/gT^2=0.018. C_{DZ} for h/gT^2=0.011 are smaller than those for another cases, but the tendency of the variation with KC_Z is in good agreement with those in other cases. Judging from these results, it can be said that the drag and inertia coefficients formulated in this study for the applicable range of the Morison equation can be applied to those in Eq.(3.16).

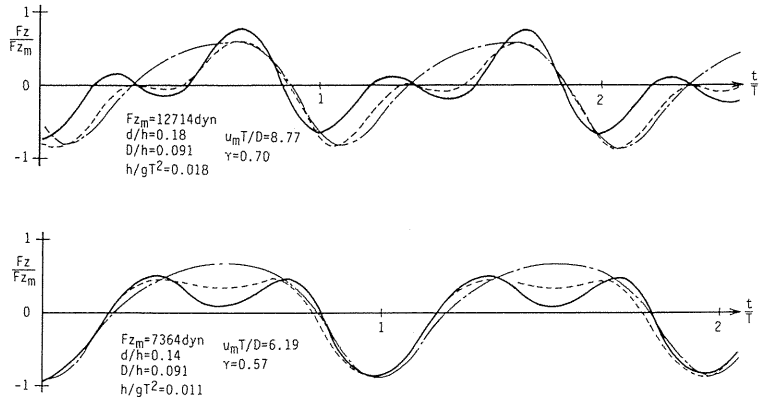

Fig. 3.23 Comparison between measured and calculated wave forces (solid line: measured, broken line : Eq.(3.16), dot-dash line : Eq.(3.3))

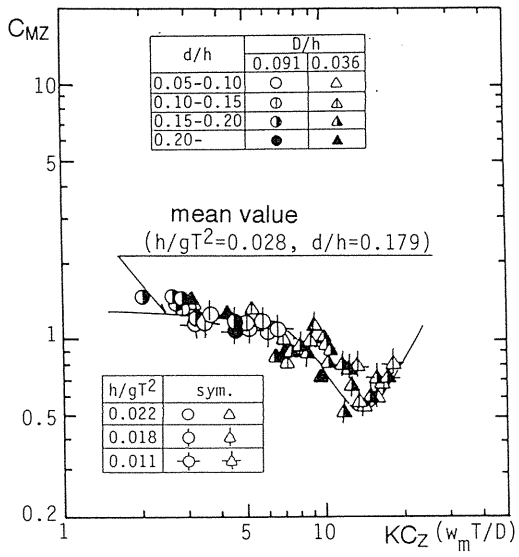

Fig. 3.24 Relationship between C_{MZ} and KC_Z

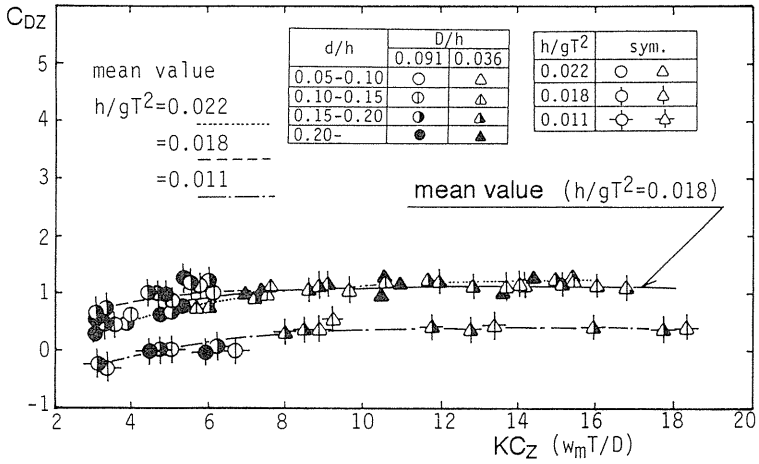

Fig. 3.25 Relationship between C_{DZ} and KC_Z

The relationship between the lift coefficient, C_{L3} and e_2/D is presented in Fig. 3.26. C_{L3} increases with an increment of e_2/D. For a fixed value of e_2/D, C_{L3} tends to be larger as

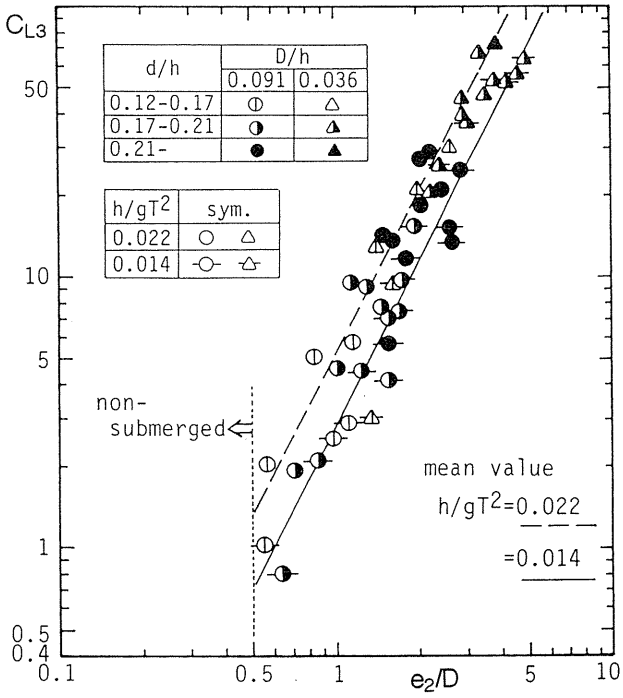

(a) h/gT^2=0.014, 0.022

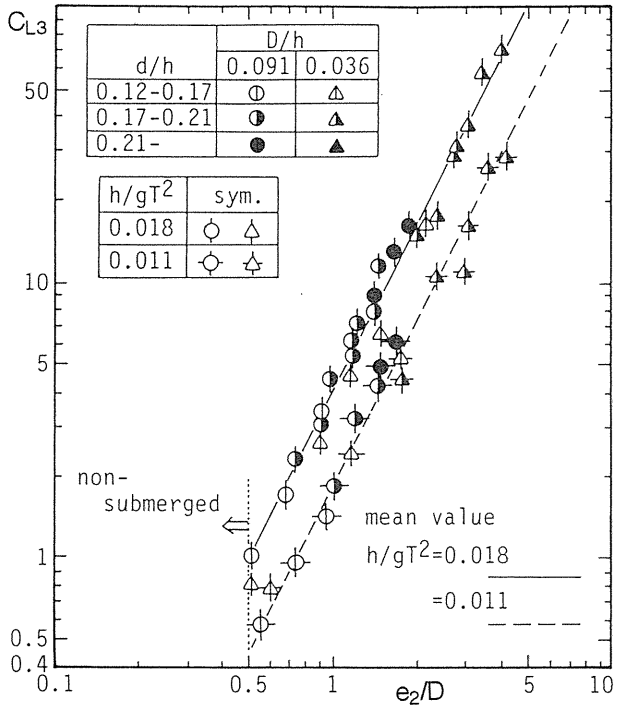

(b) h/gT^2=0.011, 0.018

Fig. 3.26 Relationship between C_{L3} and e_2/D

h/gT^2 increases. This may be due to the vertical particle motion which is not included in the lift force in Eq.(3.16). The mean value of C_{L3} can be formulated by the following equation, as shown in Fig. 3.26.

$$C_{L3} = a(e_2/D)^2 \tag{3.18}$$

where a is a coefficient and takes 5.2 for h/gT^2=0.022, 4.4 for h/gT^2=0.018, 2.8 for h/gT^2=0.014 and 1.8 for h/gT^2=0.011.

3. 9 Estimation Method of R-Type Wave Force

Estimation methods of wave forces have been discussed in the preceding sections. However, it still remains the ranges in which there is no available estimation method for the vertical wave force. In the ranges, the time history of the vertical wave force is irregular even under a regular wave train (e.g., see Fig. 3.14), because irregular vortex shedding strongly affects the wave force. This would suggest that a stochastic treatment is much superior to the deterministic method, like Morison-type equations, in the estimation of the irregular wave force. Therefore, in this section, probability distributions of the wave force and its period are discussed.

3. 9. 1 Method of Analysis

In this study, the total amplitude of the vertical wave force and its period are treated. As shown in Fig. 3.27, the period is defined as the time duration between successive two zero-up-crossing points and the total amplitude is defined as the difference between the maximum and minimum values in one period. The probability density of the dimensionless amplitude Fz_p/Fz_{rms} and its dimensionless period T_p/T are calculated, where Fz_{rms} is the rms value of Fz. The Weibull distribution is employed to express the probability distribution, since there is good agreement between the experimental results. The Weibull distribution is given in the following form.

$$p(\xi) = \frac{\beta}{\alpha}\left(\frac{\xi-\gamma}{\alpha}\right)^{\beta-1} \exp\left\{-\left(\frac{\xi-\gamma}{\alpha}\right)^{\beta}\right\} \tag{3.19}$$

where α, β and γ are the scale, the shape and the location parameters which indicate the width, the shape and the minimum value of the distribution, respectively. ξ is the variable and Fz_p/Fz_{rms} and T_p/T are taken in place. In this study, the quantities regarding the amplitude and the period are distinguished with subsuffixes F and T, respectively.

All these parameters are determined by the least square method. Figure 3.28 shows the relationship between β_T and KC_X. Most of β_T gather near 1.5, however, some of β_T scatter widely. Figure 3.29 shows two typical distributions of the period for both large and small values of β_T. The figure shows that there is no significant difference between both experimental results despite the large difference in β_T values. The best fitted Weibull distribution for large β_T, however, shows that the corresponding γ_T are too small compared with the experimental value. This would suggest that β_T is given by a constant value and the appropriate value of β_T is around 1.5. Similarly, it is confirmed that β_F is almost constant, although it scatters more than β_T. Thus, the least square fitting is performed again under the given shape parameters, β_T and β_F.

Figure 3.30 shows typical time profiles of the vertical wave forces. As shown in the figure, it is found that the time profile of the vertical wave force can be classified into two types, that is RE-type in which a similar variation is repeated and IR-type which shows a quite random variation. The RE-type wave force may occur under the influence of significant lift force but still the drag and inertia forces dominate over the lift force. The IR-type wave force is considered to be governed by the irregular lift force which dominates over the drag and inertia forces.

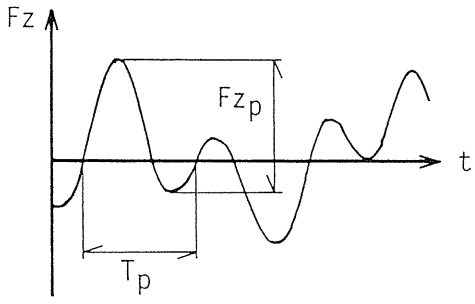

Fig. 3.27 Definition of Fz_p and T_p

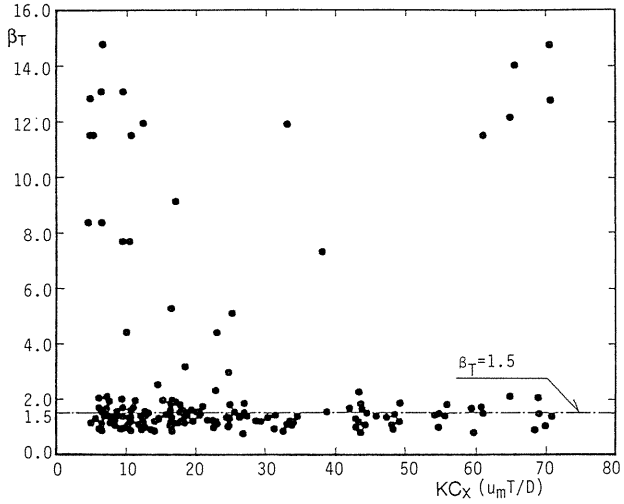

Fig. 3.28 Relationship between β_T and KC_X

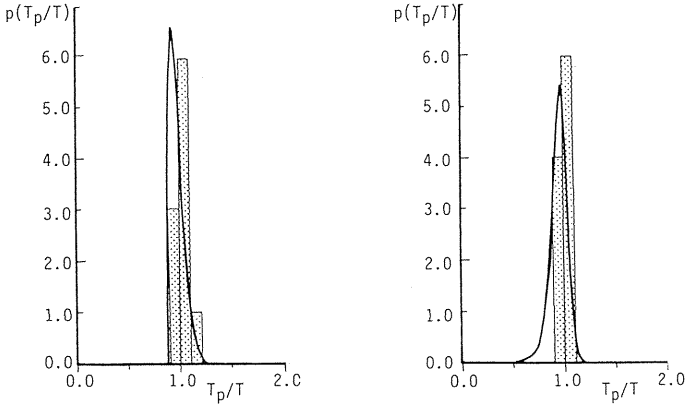

(a) β_T=1.7 (b) β_T=14.8

Fig. 3.29 Typical distributions of T_p/T

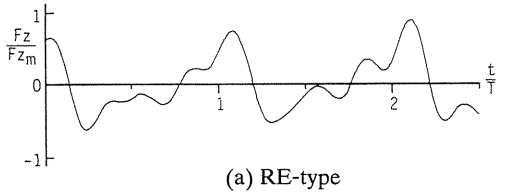

(a) RE-type

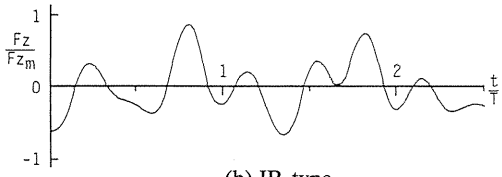

(b) IR-type

Fig. 3.30 Time profiles of R-type wave force

These types of time variation does not affect the vales of β_T and β_F, however they may affect other parameters. Thus, the least square method is performed for each type of wave force in order to discuss the properties of the Weibull parameters in detail.

3. 9. 2 Width Parameter

The relationship between α_T and KC_X is shown in Fig. 3.31. In the least square fitting, β_T is chosen as 1.26 for the RE-type and as 1.34 for the IR-type by taking the average of experimental values for each type of wave force. α_T of the RE-type is almost less than 0.1, which means that the width of distribution of the period is quite narrow. In this type of wave force, the drag and inertia forces, which have the same period as the incident wave period, are dominant components. Thus, the period of the RE-type is almost constant and equal to the incident wave period, as already discussed in Section 3.9.1. On the other hand, α_T for the IR-type is widely scattered. This implys that the period of the IR-type varies according to wave by wave. However, it can be seen from the figure that α_T converges as KC_X becomes larger. This may show that the stable vortex shedding is formed under the flow with larger KC_X than 30.

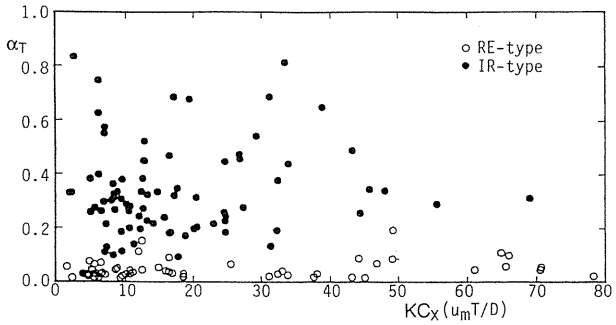

Fig. 3.31 Relationship between α_T and KC_X

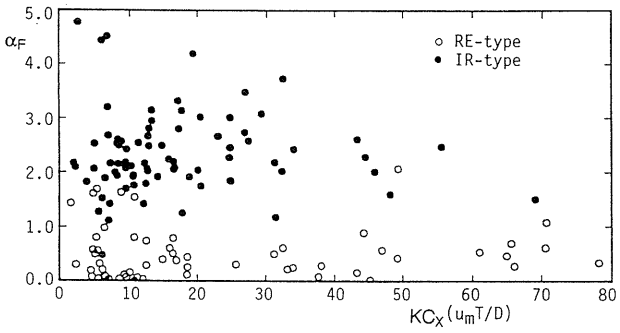

Fig. 3.32 Relationship between α_F and KC_X

The relationship between α_F and KC_X is shown in Fig. 3.32, in which β_F is chosen as 1.0 for both the RE-type and IR-type. The values of α_F of the RE-type are small and scatter a little around 0.5. This means the amplitude of the RE-type profile is quite narrow as long as the drag and inertia forces dominate over the lift force, although it is not constant because of the lift force. On the other hand, values of α_F of the IR-type is larger than those of the RE-type. That is, the width of distribution of the amplitude becomes very large when the lift force dominates over the drag and inertia forces. The distribution width of α_F seems to converge as KC_X increases. This may be due to the fact that the asymmetric vortex shedding becomes stable as KC_X increases.

3. 9. 3 Location Parameter

The relationship between γ_T and KC_X is shown in Fig. 3.33. Clear difference in γ_T between the RE-type and IR-type is confirmed. γ_T for the RE-type scatters a little around 1.0, which means that the period of the wave force coincides with the incident wave period. On the other hand, it can be seen that γ_T of the IR-type decreases with an increment of KC_X and it approaches 0.2, indicating that the period of the vertical wave force decreases with the development of the irregular vortex shedding. Thus, it can be pointed that the lift force due to the irregular vortex shedding shortens the period of the vertical wave force.

It is found that the mean value of γ_F of the RE-type is 1.43 and that of the IR-type is 0.47. As stated in Section 3.9.1, the location parameter represents the minimum wave force. Regarding the wave force, however, the value we are interested in is the maximum value. Thus, another calculation is performed using the inverse value of the non-dimensional maximum amplitude, Fz_{rms}/Fz_p. The value of the location parameter, γ_F', under this condition, gives the maximum value of the amplitude. The relationship between γ_F' and KC_X is shown in Fig. 3.34. γ_F' of the RE-type seems to be independent of KC_X and can be approximated as a constant value of 0.3. This shows that the maximum amplitude is almost three times the rms value. Regarding the values of γ_F' for the IR-type, most of them are scattered around 0.2. However, some of them are about 0.1, which means that the maximum amplitude may take about ten times the rms value of the vertical wave force.

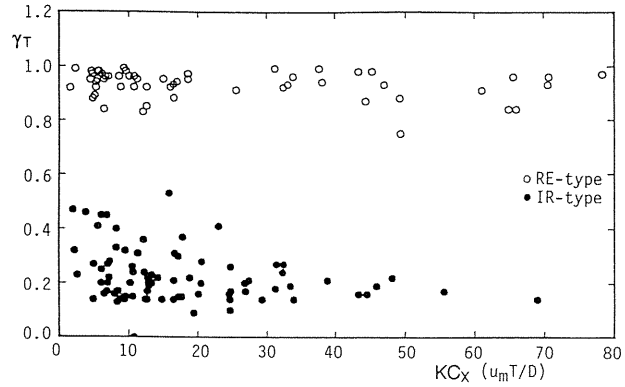

Fig. 3.33 Relationship between γ_T and KC_X

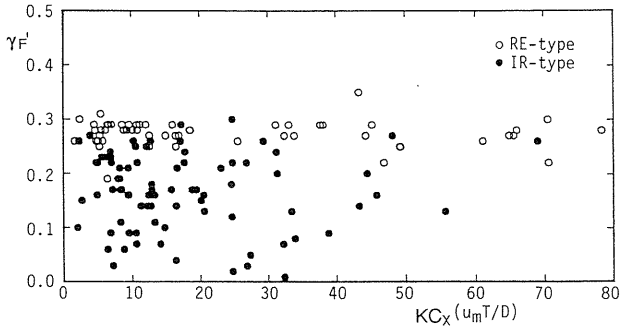

Fig. 3.34 Relationship between γ_F' and KC_X

3. 9. 4 Estimation method of Irregular Wave Force

The six parameters of the RE-type (α_T, β_T, γ_T, α_F, β_F and γ_F) are independent of KC_X and can be regarded constant. Thus, the mean probability distribution of the amplitude and the period can be determined using their mean values. Regarding the IR-type, the six parameters are scattered more than those of the RE-type, however, it is recognized that the widths of their distributions become narrow as KC_X increases. Considering that the large wave force is generated under the condition of large KC_X, the mean shape of distributions of the amplitude and the period can be also formulated using their mean values from an engineering point of view.

The mean values of the parameters of the Weibull distribution are given in Table 3.3. Using these parameters, the mean shape of the Weibull distribution can be obtained by the following expressions.

Table 3.3 Mean values of Weibull parameters

	RE-type	IR-type
α_F	0.43	2.24
β_F	1.0	1.0
γ_F	1.43	0.47
α_T	0.04	0.33
β_T	1.26	1.34
γ_T	0.94	0.23

For RE-type wave force;

$$p\left(\frac{T_p}{T}\right) = \frac{1.26}{0.04}\left(\frac{T_p/T - 0.94}{0.04}\right)^{0.26} \exp\left\{-\left(\frac{T_p/T - 0.94}{0.04}\right)^{1.26}\right\} \tag{3.20}$$

$$p\left(\frac{Fz_p}{Fz_{rms}}\right) = \frac{1}{0.43} \exp\left\{-\left(\frac{Fz_p/Fz_{rms} - 1.43}{0.43}\right)\right\} \tag{3.21}$$

For IR-type wave force;

$$p\left(\frac{T_p}{T}\right) = \frac{1.34}{0.33}\left(\frac{T_p/T - 0.23}{0.33}\right)^{0.34} \exp\left\{-\left(\frac{T_p/T - 0.23}{0.33}\right)^{1.34}\right\} \tag{3.22}$$

$$p\left(\frac{Fz_p}{Fz_{rms}}\right) = \frac{1}{2.24} \exp\left\{-\left(\frac{Fz_p/Fz_{rms} - 0.47}{2.24}\right)\right\} \tag{3.23}$$

Figure 3.35 shows comparisons between experimental and proposed distributions of Fz_p/Fz_{rms}. Although there are some discrepancies between them, the proposed model can evaluate adequately the experimental results. Thus, it can be concluded that the expected statistical values like the one-third highest and the mean vertical wave forces can be evaluated with this method.

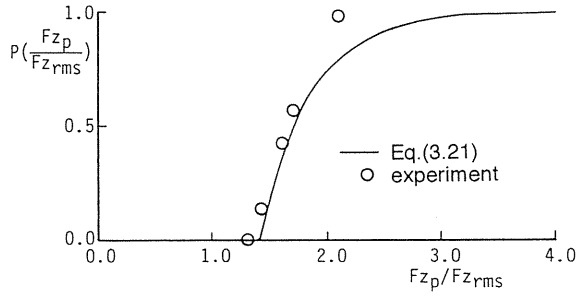

(a) RE-type

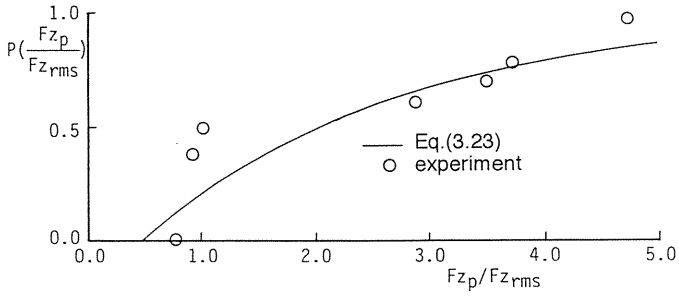

(b) IR-type

Fig. 3.35 Comparison between proposed model and experimental value

3. 10. Applicable Ranges of Wave Force Formulae

We have shown that the Morison equation, which is proposed originally for the estimation of the wave force on a vertical cylinder, is effective for a case of a submerged sphere. However, it is also revealed that this formula cannot always be applied in the evaluation of the wave force, and new formulae have been proposed in this study. For practical use, it is convenient to show the applicable ranges of these formulae graphically. Moreover, it is useful to discuss the applicable ranges of simplified formulae as well. In this section, the applicable ranges of wave force formulae and their simplified forms are discussed so that one can easily understand how to evaluate the wave force under a given condition.

In the determination of the applicable ranges, the correlation coefficients, r_M and r_D, defined by Eqs.(3.24) and (3.25) are employed.

$$r_M = \sqrt{1 - \overline{\{F_M(t) - F_T(t)\}^2}/\overline{F_T(t)^2}} \tag{3.24}$$

$$r_D = \sqrt{1 - \overline{\{F_D(t) - F_T(t)\}^2}/\overline{F_T(t)^2}} \tag{3.25}$$

where, $F_M(t)$ and $F_D(t)$ are the forces evaluated with the simplified formulae by neglecting the drag and inertia terms, respectively, and $F_T(t)$ is the wave force evaluated without any simplifications. The correlation coefficient of 0.9 is chosen as the critical value, which is the same value that determines the applicable range of the Morison equation.

Summarizing these results, Figs. 3.36 and 3.37 are obtained. In the figures, the wave breaking condition was calculated with Miche's breaking limit. Similar figures are obtained for different conditions, however they are not shown here because of the limited space.

The critical value of KC_X of the applicable range of the inertia and drag terms for F_X are almost constant, that is KC_X=7 and =30, respectively. On the other hand, in the case of F_Z, they are not constant, but decrease with an increment of submergence depth of the sphere. This is due to the contribution of horizontal water particle motion to the drag term.

From Fig. 3.12, which shows the relationships between the non-dimensional maximum wave force and KC_X, it is clear that the inertia force is much larger than the drag force when KC_X is less than 7. Conversely, the drag force greatly dominates the inertia force when KC_X is larger than 30. This presents that the critical lines in Fig. 3.36 adequately show the range in which either the inertia term or the drag term can be neglected in estimating the wave force.

Regarding the vertical wave force, the validity of the critical lines in the Fig. 3.37 can also be confirmed from Fig. 3.13.

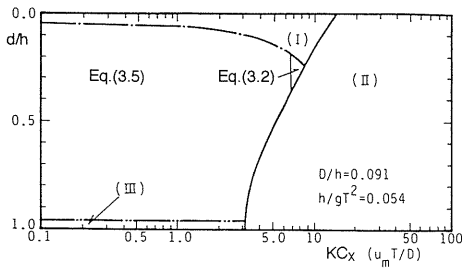

(a) h/gT^2=0.054, D/h=0.091

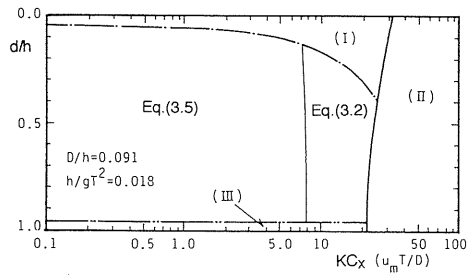

(b) h/gT^2=0.018, D/h=0.091

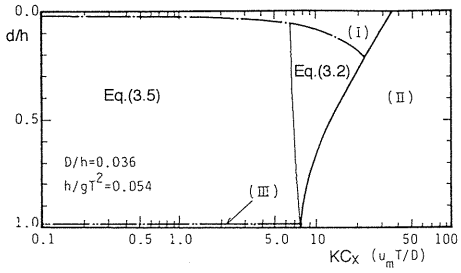

(c) h/gT^2=0.054, D/h=0.036

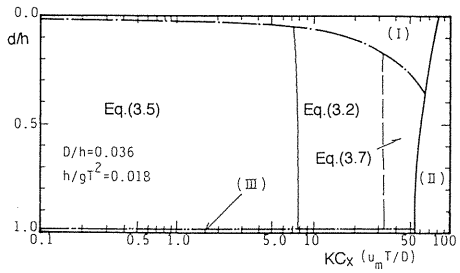

(d) h/gT^2=0.018, D/h=0.036

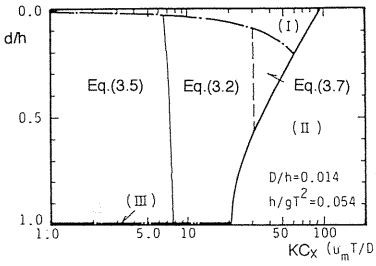

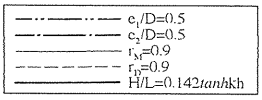

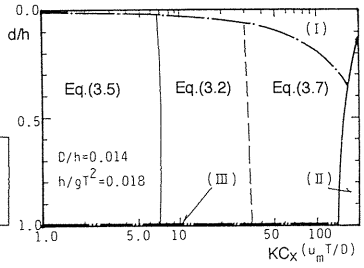

(e) h/gT^2=0.054, D/h=0.014

(f) h/gT^2=0.018, D/h=0.014

Fig. 3.36 Applicable ranges of wave force formulae for Fx
((I): non-submerged, (II): no waves, (III): on bottom)

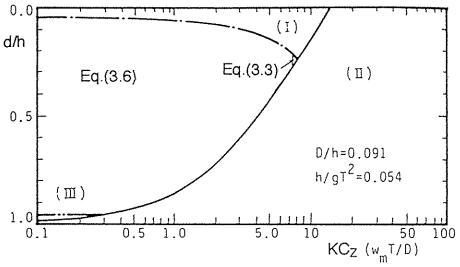

(a) h/gT^2=0.054, D/h=0.091

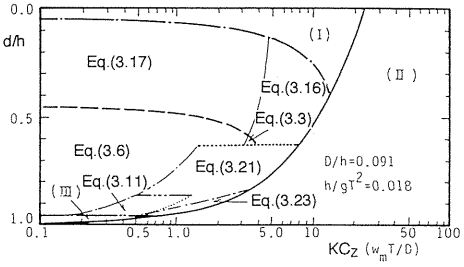

(b) h/gT^2=0.018, D/h=0.091

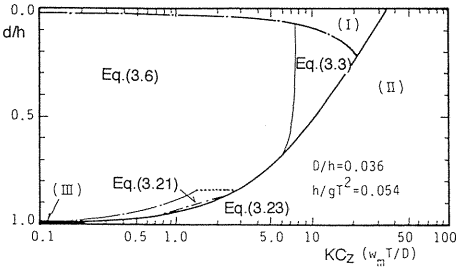

(c) h/gT^2=0.054, D/h=0.036

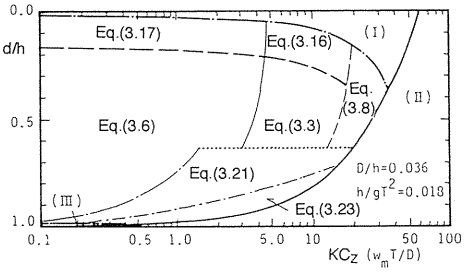

(d) h/gT^2=0.018, D/h=0.036

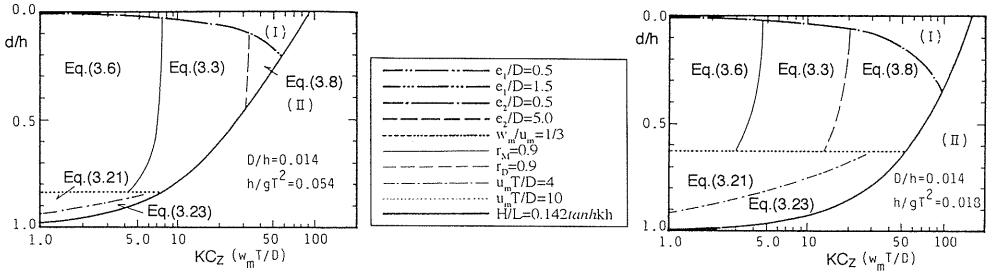

(e) h/gT^2=0.054, D/h=0.014 (f) h/gT^2=0.018, D/h=0.014

Fig. 3.37 Applicable ranges of wave force formulae for Fz
((I): non-submerged, (II): no waves, (III): on bottom)

3. 11 Conclusions

1) The wave-induced flow around the sphere can be classified into four types, such as the oscillating patterns with and without the flow separations and the rotating patterns with and without the flow separations, and their appearance ranges are revealed.
2) In the unseparated flow, the maximum wave force is proportional to the wave height. On the other hand, the maximum wave force is in proportion to the squared wave height when the flow is separated.
3) New equations to evaluate the vertical wave force affected by the bottom and free surface boundary proximity are proposed. These equations estimate well the measured wave force affected by the boundary proximity effects.
4) The inertia and drag coefficients in applicable range of the Morison equation, and the lift coefficients for proposed formulae are formulated graphically.
5) The applicable ranges of the wave force formulae and their simplified forms are shown graphically.

4. Concluding Remarks

The wave forces acting on a submerged sphere in the regular wave field have been discussed theoretically and experimentally in this paper. When the size of a sphere is large compared with the wavelength, the diffraction force is dominant. The diffraction force can be evaluated by means of numerical analysis and the Source Distribution Method (the SDM) based on the linear wave theory is shown to be useful method with enough accuracy, except for the vertical force on a sphere which emerges from the wave trough. The ranges in which the diffraction force is dominating have been shown based on the numerical analysis.

For the case of a small sphere, the Morison equation is applicable in estimating the horizontal wave force. In its application, the drag and inertia coefficients should be carefully chosen. This study gives such coefficients as a function of KC_X and h/gT^2. In the estimation of the vertical wave force, the Morison equation cannot always be applied and its applicable ranges is revealed. For the vertical wave forces in inapplicable range, the new estimation methods are proposed. Moreover, the wave force coefficients of these formulae are also

formulated. For practical application of these estimation methods, some simplifications without lacking accuracy are possible. This study has also investigated the applicability of simplified formulae.

The accumulated knowledge about the wave force on a submerged sphere by past research has been limited and not been enough to reflect on the practical design. This study covers over whole ranges in which the diffraction force is essentially important and the drag and inertia and lift forces are dominant and compensates the shortage of past research. Thus, it enables the designers and field engineers to evaluate the wave force acting on a submerged sphere.

References

1) Chakrabarti, S.K.: In-line forces on fixed vertical cylinder in waves, Journal of Waterway, Port, Coastal and Ocean Division., Proceedings of ASCE, Vol.106, No.WW2, pp.140–155, 1980.
2) Kono, T.: Fundamental study on the vibration of submerged structure caused by surface waves, Bulletin of Ryukyu University, Vol.5, pp.129–212, 1974. (in Japanese)
3) Jenkins, S.A. and Inman,D.L.: Forces on a sphere under linear progressive waves, Proceedings of the 15th International Conference on Coastal Engineering, pp.2413–2428, 1976.
4) Grace, R.A. and Cassiano, F.M.: Ocean wave force on a subsurface sphere", Journal of Waterways and Harbors Division, Proceeding of ASCE, Vol.95, No.WW3, pp.291–317, 1969.
5) Havelock,T.H.: The wave forces on a submerged body moving under waves, Quarterly Transactions of Naval Architect, January, and in The Collected Papers of Sir Thomas Havelock on Hydrodynamics, ONR/ACR-103, pp.590–596, 1954
6) Garrison, C.J. and Rao, V.S.: Interaction of waves with submerged objects, Proceeding of ASCE, Vol.97, No.WW2, pp.259–277, 1971.
7) Chakrabarti, S.K. and Naftzger, R.A.: Nonlinear wave forces on half-cylinder and hemisphere, Proceedings of ASCE, Vol.100, No.WW3, pp.189–204, 1974.
8) Black, J.L.: Wave forces on vertical axisymmetric bodies, Journal of Fluid Mechanics, Vol.67, Part 2, pp.369–376, 1975.
9) Fenton, J.D.: Wave forces on vertical bodies of revolution, Journal of Fluid Mechanics, Vol.85, pp.241–255, 1978.
10) John, F.: On the motion of floating bodies.II, Communications on Pure and Applied Mathematics, Vol.13, pp.45–101, 1959.
11) Mizutani, N., Iwata, K. and Matsuoka, S.: Wave diffraction and forces acting on a spherical structure, Coastal Engineering in Japan, Vol.34, No.1, pp.31–49, 1991.
12) Morison, J.R., O'Brien, M.P., Johnson, J.W. and Schaaf, S.A.: The wave force exerted by surface wave on piles, Petroleum Transactions, AIME, Vol.189, pp.149–157, 1950.
13) Keulegan, G.M. and Carpenter, L.H.: Forces on cylinders and plates in an oscillating fluid, Journal of Research of the National Bureau of Standards, Vol.60, No.5, pp.423–440, 1958.
14) Nakamura, H., Ikeda, S. and Oyagi, T.: Forces on spheres in sinusoidally oscillating flows –a continued report–, Proceedings of the 30th Japanese Conference on Coastal Engineering, pp.381–384, 1983. (in Japanese)
15) Uekita, Y. and Yamazaki, H.: Wave force on submerged horizontal cylinder, Proceedings of the 27th Japanese Conference on Coastal Engineering, pp.358–362, 1980. (in Japanese)
16) Sarpkaya, T.: Forces on cylinders and sphere in a sinusoidal oscillating fluid, Journal of Applied Mechanics, Transactions of ASME, Vol.42, pp.32–37, 1975.
17) Iwata, K. and Mizutani, N.: Vortex formation and shedding around a submerged sphere under wave action, Proceedings of the 1st Pacific/Asia Offshore Mechanics Symposium, Vol.2, pp.205–211, 1990.
18) Lamb, H.: Hydrodynamics (6th edition), Cambridge University Press., 738p, 1932.

19) Iwata, K. and Mizutani, N.: Proximity effects of bottom and free surface boundaries to wave force acting on a submerged sphere, Proceedings of the 1st Offshore and Polar Engineering Conference, Vol.3, pp.164–171, 1991.
20) Iwata, K., Mizutani, N. and Kawasumi, N.: Effects of the free surface proximity to wave forces acting on a submerged sphere, Proceedings of Coastal Engineering, JSCE, Vol.36, pp.724–728, 1989. (in Japanese)
21) Kim, W.D.: Nonlinear free-surface effect on a submerged sphere, Journal of Hydronautics, Vol.3, No.1, pp.29–37, 1969.